European Journal of Medicinal Chemistry 304 (2026) 118494

Contents lists available at ScienceDirect

European Journal of Medicinal Chemistry

journal homepage: www.elsevier.com/locate/ejmech

Research paper

In vitro kinetic profiling by enzymatic approaches to select FAPIs with a long residence time

Emile Verhulst [a], Pawel Brzeminski [b], Anke de Groot [a], Joep W. Wals [b], Robbe Michiels [a], Adrian Fabisiak [b], Jari Thys [a], Sergei Grintsevich [b], Yentl Van Rymenant [a], Sarah Peeters [b], Stijn Lambregts [b], Yani Sim [a], Ruben Verstraete [c], Pieter Van Wielendaele [a], Maya Berg [d], Filipe Elvas [e], Xaveer Van Ostade [c], Frank Rösch [f], Anne-Marie Lambeir [a,d], Hans De Winter [b], Pieter Van Der Veken [b,d], Ingrid De Meester [a,d,*]

[a] Laboratory of Medical Biochemistry, Faculty of Pharmaceutical, Biomedical and Veterinary Sciences, University of Antwerp, Wilrijk, 2610, Belgium
[b] Laboratory of Medicinal Chemistry, Faculty of Pharmaceutical, Biomedical and Veterinary Sciences, University of Antwerp, Wilrijk, 2610, Belgium
[c] Cell Death Signaling–Proteomics Team, Faculty of Pharmaceutical, Biomedical and Veterinary Sciences, University of Antwerp, Wilrijk, 2610, Belgium
[d] Infla-Med Centre of Excellence, University of Antwerp, Wilrijk, 2610, Belgium
[e] Molecular Imaging and Radiology, Faculty of Medicine and Health Sciences, University of Antwerp, Wilrijk, 2610, Belgium
[f] Department of Chemistry–TRIGA Site, Johannes Gutenberg University Mainz, Mainz, 55128, Germany

ARTICLE INFO

Keywords:
FAP
FAPI
Radioligand
Enzyme kinetics
Jump-dilution assay
Residence time
Molecular docking

ABSTRACT

Fibroblast activation protein α (FAP) is a transmembrane serine protease overexpressed in cancer-associated fibroblasts and implicated in tumor progression and fibrosis. Although several FAP inhibitors (FAPIs) show excellent tumor uptake for positron emission tomography (PET) imaging, rapid target dissociation often limits tumor retention and constrains their use in theranostic radioligand therapy. Considerable effort is directed toward FAPI radioligands with prolonged tumor residence time, yet a validated, medium-throughput *in vitro* method to estimate FAPI-target residence time remains lacking, hindering correct prioritization of lead radioligands for preclinical evaluation. In this study, we employ a jump-dilution assay to determine the dissociation rate constant (k_{off}) of FAPIs under tight-binding conditions, providing a direct handle on drug-target residence time ($\tau = 1/k_{off}$). We combine this assay with progress-curve assays to determine the association rate constant (k_{on}) and inhibition constant (K_i). By resolving binding kinetics, especially k_{off}, this approach addresses limitations of conventional IC_{50}-based screening, offering a finer discrimination among leads and enabling data-driven ranking based on target residence time. We demonstrate the utility of this workflow through a kinetic structure-activity relationship (SAR) analysis on FAPIs with varying structural features and warhead chemistries (carbonitrile, α-ketoamide). Molecular docking studies allowed us to correlate experimental kinetic parameters with predicted binding modes within the three-dimensional structure of FAP, focusing on critical interactions within the active site. These findings highlight the value of kinetic profiling in FAPI development and support the rational design of theranostic agents with prolonged target retention.

1. Introduction

Fibroblast activation protein α (FAP) is a glycosylated type II transmembrane serine protease that is minimally expressed in most healthy adult tissues [1–4], yet is markedly upregulated in specific pathological contexts. Elevated FAP expression is a hallmark of activated fibroblasts in the tumor microenvironment [1,5,6], fibrotic tissues [7–9] and wounds [1]. Its consistent overexpression in over 90 % of epithelial carcinomas and at sites of active tissue remodeling has positioned FAP as a key player in tumor pathophysiology [1,10]. In malignancy, FAP's involvement in extracellular matrix remodeling and tissue repair processes facilitates tumor invasion and metastasis [11]. FAP features a short intracellular tail (aa 1–4) [12,13] and transmembrane domain (aa 5–25), followed by a large C-terminal extracellular domain (aa 26–760)

* Corresponding author. Laboratory of Medical Biochemistry, Faculty of Pharmaceutical, Biomedical and Veterinary Sciences, University of Antwerp, Wilrijk, 2610, Belgium.
E-mail address: ingrid.demeester@uantwerpen.be (I. De Meester).

https://doi.org/10.1016/j.ejmech.2025.118494
Received 24 September 2025; Received in revised form 28 November 2025; Accepted 12 December 2025
Available online 18 December 2025

containing the active site (Fig. S1). Membrane-attached FAP can be cleaved to produce a soluble form – known as antiplasmin-cleaving enzyme (APCE) [14,15] – which is detectable in plasma, although its origin remains unclear [16–19].

FAP combines two key features that make it an attractive pan-tumor target in oncology: (i) selective expression by cancer-associated fibroblasts (CAFs), with negligible levels in healthy tissues, and (ii) an easily accessible, extracellular active site [12]. Early efforts to exploit FAP in cancer therapy centered on antibody-based agents and first-generation small-molecule inhibitors [20], but many candidates underperformed in preclinical or clinical testing due to off-target toxicity or insufficient antitumor efficacy [21–24]. A breakthrough came with the development of the quinoline-based FAP inhibitors (FAPIs) [25–27]. When converted into PET imaging tracers, these FAPIs demonstrated outstanding sensitivity and contrast, reliably delineating tumor margins and revealing metastatic lesions in both preclinical models and early human studies [28–30]. Their remarkable diagnostic performance prompted a surge of academic and pharmaceutical interest, accelerating (pre-)clinical development and paving the way for routine clinical use of FAP-targeted PET tracers in tumor diagnosis in the (very) near future [31–40].

Yet the very properties that make these tracers ideal for imaging – rapid tumor uptake with fast blood clearance and washout from non-target tissues – do not ensure the prolonged intratumoral retention required for therapy, where sustained retention in the tumor stroma is needed for adequate dose delivery. Consequently, there is a growing impetus within the field to design FAP radioligands that leverage high affinity with extended tumor retention [32,41]. Strategies under investigation include scaffold modifications to slow dissociation, albumin-binding motifs to extend serum half-life, multimerization to exploit valency effects, and peptide (including cyclic-peptide) designs to modulate binding kinetics [42–51]. Identifying a radioligand that unites high affinity with optimal pharmacokinetics and prolonged tumor retention would enable practical theranostic use, i.e., deployment of the same scaffold for high-contrast PET imaging and for targeted radionuclide therapy [52,53]. Importantly, the inherent fast systemic clearance of small-molecule FAP ligands helps preserve favorable therapeutic indices by limiting normal-organ dose, especially when intratumoral retention is long [30,54]. FAPIs with prolonged tumor retention could thus serve as vehicles for targeted drug delivery, maximizing therapeutic efficacy while minimizing systemic toxicity [38,55,56].

Prolonged tumor retention remains the primary challenge. Yet many preclinical investigations still rely on static binding affinity (IC_{50}) to screen experimental FAPIs, which fails to capture the dynamic FAP-FAPI interplay that governs *in vivo* performance [57–63] and loses discriminating power under 'tight-binding' conditions. In contrast, the dissociation rate constant k_{off} – the reciprocal of target residence time (τ) – quantifies the duration a molecule remains bound to its target and is emerging as a critical parameter alongside tumor uptake [63–67]. A longer τ correlates with sustained *in vivo* target occupancy, reduced dosing frequency, and enhanced therapeutic selectivity, ensuring efficacy even as plasma levels fluctuate [68,69]. At the same time, a high association rate constant (k_{on}) supports rapid target engagement and helps maintain effective FAPI concentrations at the tumor site [57,61,70].

Existing methods fail to reliably measure k_{off}, or lack the throughput needed to cover the growing range of candidate molecules [71]. This underscores the need for assay development that balances accurate determination of k_{off} with practical applicability. Improved biochemical tools for τ evaluation are essential to reduce the risks and costs associated with preclinical development [71]. Jump-dilution assays (JDAs) are well-established methods to determine the reversibility of an inhibitor [72], but can also be used for the determination of k_{off}. In this work, we adjusted regular JDA workflows for slow tight-binding conditions and applied them to a systematic screening of a range of experimental in-house developed FAPIs. Complementary progress curve assays provide additional information on k_{on} and the inhibition constant (K_i) of these FAPIs. These methods offer mechanistic insight while maintaining a relatively high experimental throughput [62,71,73]. To illustrate this approach, this study undertakes a kinetic structure-activity relationship (SAR) of a panel of FAP inhibitors differing in warhead type and key structural substituents. For a subset of compounds, we include an illustrative docking analysis to examine whether lower k_{off} coincides with more favorable active-site fits.

In this study, we establish an operational framework for determining dissociation kinetics of FAPIs under slow, tight-binding conditions. Using a JDA tailored to FAP and complemented with progress curve analyses, we generate reliable estimates of k_{off}, k_{on} and, where informative, K_i across a chemically diverse panel of FAPIs. This workflow enables systematic kinetic comparison of inhibitors and provides a practical means to quantify target residence time, an emerging parameter of interest in the design of FAP-targeted radioligands. This kinetic framework lays the foundation for selecting candidates with durable target occupancy, while future cellular and *in vivo* studies will be required to validate how these kinetic features translate into biological performance.

2. Methods

2.1. Chemistry

FAP inhibitor (FAPI) **1** was prepared as described by Tanc et al. [37], while FAPIs **3**, **22**, **23**, **24** and **25** were obtained as described before [74]. Reference FAPI **6d** from Šimková et al. was synthesized as described by Šimková et al. [75]. α-ketoamide derivatives **2**, **6**, **7**, **8**, **9**, **10**, **11**, **12**, **13**, **14**, **15**, **16**, **17**, **18**, **19**, **20**, **21**, **29**, **30**, **31**, **32**, **33**, **34**, **35** were prepared as described previously [76,77]. **[^{18}F] AlF-FAPI-74** was obtained as described by Naka et al. [78]. **DOTAGA.Glu.(FAPi)$_2$** and **^{nat}Lu-DOTAGA.Glu.(FAPi)$_2$** were prepared as reported by Martin et al. [35]. Finally, **FAP-2286** was obtained from BLDpharm (Cat. No. BD01611490) and **^{nat}Lu-FAP-2286** was obtained according to Osterkamp et al. [79,80].

Sulfonamide FAPIs **26**, **27**, **28** were synthesized as outlined in Scheme S1. For this, compound **A** was first deprotected using *p*-TsOH·H_2O, and the resulting intermediate was subsequently coupled with compound **B** to afford product **C**. The obtained product was then methylated to yield the quaternary ammonium salt **D**. Finally, acidic removal of the tert-butyloxycarbonyl (Boc)-protecting group furnished the corresponding amine, which was subjected to the reaction with corresponding sulfonamide to afford the target FAPIs **26**, **27**, **28**. A detailed protocol can be found in the supplementary material & methods (Supplementary File 4.1: Chemistry; Scheme S1; Figs. S2–S9).

2.2. FAP expression construct design

A construct encoding soluble FAP (residues 26–760) without the N-terminal cytosolic tail (residues 1–4) and transmembrane domain (residues 5–25) was designed in-house and ordered from Genscript. It constitutes the α/β-hydrolase domain (residues 26–53 and 493–760) where the catalytic triad (Ser624 - Asp702 - His734) resides [81,82], and a β-propeller domain (residues 54–492) that plays a role in dimerization and substrate specificity [81,83]. The final construct contained an N-terminal μ-phosphatase secretion leader peptide (MGILPSPGMPALLSLVSLLSVLLMGCVAE), and a C-terminal HRV3C cleavage site, 8xHis-tag, and TwinStrep® tag. The engineered recombinant human FAP (rhFAP) protein expression construct is available on Addgene (plasmid no. 239817). The plasmid containing the FAP gene (aa 26–760) was transformed into *E. coli* TOP10F' cells (Thermo Fisher Scientific, Cat. No. C303003) to amplify recombinant plasmid DNA, and the Plasmid Maxi Kit (Qiagen, Cat. No. 12163) was used to isolate the plasmid DNA.

2.3. Expression of FAP in Freestyle™ 293-F cells

Freestyle™ 293-F cells (Thermo Fisher Scientific, Cat. No. R79007) were cultured in Freestyle™ 293 medium (Thermo Fisher Scientific, Cat. No. 12338018) on an orbital shaker (105 rpm, 37 °C, 5 % CO_2), for at least three passages. The cells were transfected at a density of $\pm 1 \times 10^6$ cells per mL with 1 μg plasmid DNA and 2 μg Lipofectamine 2000 (Thermo Fisher Scientific, Cat. No. 11668019) per mL of cells. PenStrep (Thermo Fisher Scientific, Cat. No. 15140122) was added to the cell culture 4 h after transfection at a final concentration of 100 units/mL penicillin and 100 μg/mL streptomycin to prevent contamination.

2.4. Purification of FAP

Cell culture medium containing the final secreted protein product FAP(26–760)-HRV3C-8xHis-TwinStrep® (pI: 6.2) was collected by sequential centrifugation (5 min, 4 °C, 1000×*g* & 20 min, 4 °C, 18,000×*g*) approximately 5–6 days post-transfection when cell viability dropped to 75 %. The centrifuged medium was filtered through a 0.22 μm filter and adjusted to pH 8 by addition of sample preparation buffer (500 mM Tris, 750 mM NaCl, 5 mM EDTA, pH 8) in a 1:5 ratio, before loading the buffered cell culture medium onto a StrepTrap XT column (Cytiva, Cat. No. 29401317) equilibrated with equilibration buffer (100 mM Tris, 150 mM NaCl, 1 mM EDTA, pH 8). The protein was eluted isocratically with elution buffer (100 mM Tris, 150 mM NaCl, 1 mM EDTA, pH 8, 2.5 mM d-Desthiobiotin; Sigma-Aldrich, Cat. No. D1411-500 MG). Elution was paused for 10 min when the peak was reached, resulting in a more concentrated elution thereafter. Elution samples were pooled, slightly concentrated to a volume ≤3 mL using a 30K Amicon® Ultra Centrifugal Filter (Merck, Cat. No. UFC9030) and subsequently loaded onto a HiLoad 16/600 Superdex™ 200 pg column (Cytiva, Cat. No. 28989335) for size-exclusion chromatography in a buffer composed of 50 mM Tris, 150 mM NaCl, 2 % glycerol, pH 7.5. The peak fractions were then checked for protein purity via SDS-PAGE and concentrated to a protein concentration of 1 mg/mL using a centrifugal concentrator. Purified protein samples were aliquoted at the same concentration and stored at −80 °C in the same buffer.

Protein content was assessed according to the method of Bradford et al. using bovine serum albumin (BSA, Thermo Fisher Scientific, Cat. No. 240401000) as a standard. A total of 10 μL of sample was added to a 96-well microplate followed by 100 μL of Bradford reagent [84]. The absorbance was measured at 595 nm (SpectraMax Plus 384, SoftMax Pro v7.0.3. software, Molecular Devices) and protein concentration was determined from the BSA standard curve.

2.5. Protein quality control

2.5.1. Liquid chromatography and mass spectrometry

Ten μg of purified FAP were separated by SDS-PAGE and visualized with Coomassie staining. Visible bands were excised and subjected to in-gel Trypsin (Thermo Fisher Scientific Cat. No. 90305) digestion, following the protocol described by Shevchenko et al. [85]. Resulting peptides were analyzed using an UltiMate 3000 (Dionex) Ultra-Performance Liquid Chromatography (UPLC) system, employing a trap-and-elute configuration. Peptides were initially loaded onto a PepMap100C18 trap column and subsequently separated on a 50 cm PepMap Neo C18 analytical column (75 μm i.d., 2 μm particle size), using a 40-min gradient ranging from 5 % to 40 % solution B (80 % ACN, 0.08 % FA in ultrapure water), followed by 95 % ACN in 0.1 % formic acid, at a flow rate of 0.3 μL/min. Eluted peptide fractions were introduced into a Fusion Orbitrap mass spectrometer (Thermo Fisher Scientific) via a Nanospray Flex™ ESI source (1.9 kV), operating in positive ion mode. Full MS scans (*m/z* 350–2000) were acquired in the Orbitrap at a resolution of 120,000. Precursors with charge states 2–6 were selected for MS2 fragmentation by CID (30 % collision energy) and measured at 60,000 resolution. Dynamic exclusion was set to 60 s, with an intensity threshold of 2.5e4 and a 1.6 *m/z* isolation window. Raw data were processed using MaxQuant (version 2.0.1.0). Protein identification was performed using the Swiss-Prot human database, allowing up to two missed cleavages. Methionine oxidation and N-terminal acetylation were considered variable modifications; carbamidomethylation of cysteine was set as a fixed modification. Searches were run with standard Orbitrap settings. Full protocol can be found in SI (4.4).

2.5.2. N-glycosylation

Recombinant FAP was deglycosylated by PNGase F under conditions optimized for detection by western blotting. For each reaction, ≥3.5 μg of FAP was diluted in a 10 μL mixture containing 1 μL of 10x Glycoprotein Denaturing Buffer (NEB, Cat. No. P0704S) and water as needed. Samples were denatured by heating at 100 °C for 10 min, then immediately chilled on ice and briefly centrifuged (10 s). The denatured sample was then brought to a final reaction volume of 20 μL by adding 2 μL of glycobuffer 2 (NEB, Cat. No. P0704S), 2 μL of 10 % NP-40 (NEB, Cat. No. P0704S), 1 μL of PNGase F (NEB, Cat. No. P0704S) and water as needed. Each dilution was prepared in duplicate, with one aliquot receiving PNGase F treatment and the other serving as a control. The reactions were incubated at 37 °C for 1 h and 10 μL of each reaction was loaded onto a 7.5 % SDS-PAGE gel. Deglycosylation was verified by comparing mobility shifts of the treated versus control samples.

2.5.3. Differential scanning fluorimetry

FAP was concentrated to 50 μM using a 30K Amicon® Ultra Centrifugal Filter (Merck, Cat. No. UFC9030) at 14,000 g and 4 °C. A salt reduction step was performed using ultrapure water under the same centrifugation conditions. Assay mixtures were prepared in a 96-well PCR plate according to the manufacturer's protocol, yielding a final concentration of 4 μM rhFAP with a 10:1 dye-to-protein ratio. Differential scanning fluorimetry was conducted on a CFX Connect™ RT-PCR system (Bio-Rad, USA) using a temperature gradient of 1.0 °C/min from 25 °C to 95 °C, with fluorescence measurements recorded every 30 s. All conditions were tested in duplicate. The melting temperature (T_m) was determined by analyzing the first derivative of the fluorescence intensity versus temperature curve, specifically looking for the peak in the derivative plot, which corresponds to the inflection point of the original curve. Data processing and visualization were performed using Python® (version 3.11) packages pandas, matplotlib, and seaborn.

2.6. In vitro enzymatic activity assays

All *in vitro* enzyme assays were performed following a standardized workflow; any assay-specific modifications are detailed in the respective assay descriptions below. Stock solutions of enzyme (in buffer), inhibitors (in DMSO), and substrate (in methanol) were prepared and subsequently diluted with assay buffer (50 mM Tris, 140 mM NaCl, 1 mg/mL BSA, pH 8) to generate the working solutions. All components were prewarmed to 37 °C prior to measurement, and the order and timing of additions were optimized on a per-assay basis. All assays were carried out in 96-well reaction plates (transparent, flat bottom, half-area; Greiner Bio-One, Cat. No. 675101) using an Infinite M200 or F200 Pro microplate reader (Tecan, Switzerland) and the Magellan software (v7.2). Unless otherwise specified, all measurements were conducted at 37 °C, and all data were corrected using an appropriate blank (i.e. reaction mixture without enzyme). Each experiment was performed in triplicate, unless otherwise specified. Specific definitions for commonly encountered kinetic and equilibrium constants can be found in Pinto et al. Table 2 [86]. Substrates used in the assays below are N-Carbobenzoxyglycyl-prolyl-4-methylcoumarinyl amide (ZGP-AMC; substrate **A**), N-(2-oxo-2-[(S)-2-(N-4-methyl-7-coumarinylcarbamoyl)-1-pyrrolidinyl]ethyl)-4-quinolinecarboxamide (substrate **B**; De Decker et al. compound 6a [87]) and N-[(R)-2-[(S)-4,4-difluoro-2-(N-4-methyl-7-coumar-

inylcarbamoyl)-1-pyrrolidinyl]-1-methyl-2-oxoethyl]-4-quinolinecarboxamide (substrate **C**; De Decker et al. compound 6c [87]). An overview of the obtained Michaelis-Menten substrate parameters (k_{cat}, K_m) can be found in Table S3, Figure S14 and Figure S15. Different substrates were used in specific assays due to availability at the time of the experiments.

2.6.1. Active site titration

Ideally, an irreversible inhibitor would be used for this experiment; however, in its absence, we employed a very tight-binding inhibitor with a low k_{off} (FAPI **5**). Reaction mixtures were prepared with varying inhibitor concentrations: 4.0 nM, 2.0 nM, 1.0 nM, 0.50 nM, 0.25 nM, 0.13 nM, 0.06 nM, and 0.03 nM FAPI **5**, incubated with 1.0 nM rhFAP for 30 min at 37 °C to promote enzyme-inhibitor complex formation. Immediately before measurement, prewarmed substrate A was added to a final concentration of 150 μM. Fluorescence was recorded kinetically for 10 min. Data were analyzed in GraphPad Prism via simple linear regression of the initial reaction velocities (v_i), normalized to the uninhibited control (v_0), where the x-intercept of the regression line corresponds to the concentration of catalytically active FAP subunits.

2.6.2. IC_{50} with varying rhFAP concentration

Half-maximal inhibitory concentration (IC_{50}) values were determined using the fluorogenic substrate ZGP-AMC at a final concentration of 150 μM to ensure sufficient signal at the lowest FAP concentrations. Inhibitors were prepared as a ten-point serial dilution (400 nM–0.0015 nM), and 5 μL of each dilution was added to the wells. Twenty μL of rhFAP at the indicated final concentrations (0.1, 0.3, 0.9 or 2.7 nM) were added, followed by a 15 min preincubation at 37 °C. Reactions were initiated by addition of pre-warmed substrate to a final volume of 50 μL, and fluorescence was recorded at 37 °C for at least 20 min. Initial rates were extracted from the linear portion of the progress curves, normalized to the positive (no-inhibitor) control, and fitted with a four-parameter logistic equation to obtain IC_{50} values (GraphPad Prism). All measurements were performed in duplicate and are reported as mean ± SEM.

2.6.3. Kinetic binding schemes

Under standard assumptions, an enzyme-inhibitor system is considered to reach equilibrium rapidly, effectively within the mixing time of the experiment. For slow-binding inhibitors, however, equilibration occurs on the experimental timescale and can occur via several mechanisms. The two most commonly encountered are a one-step mechanism (Scheme A), or a two-step mechanism in which the rapid formation of the initial enzyme-inhibitor complex is followed by a slow step leading to the final enzyme-inhibitor complex (Scheme B). In these schemes, k_{on} and k_{off} describe formation and dissociation of the encounter complex EI in the one-step reaction; whereas k_1 and k_{-1} describe the formation and dissociation of the encounter complex EI in the two-step reaction, and k_{for} and k_{rev} describe the reversible conversion between EI and EI*.

$$E + I \underset{k_{off}}{\overset{k_{on}}{\rightleftharpoons}} E{\cdot}I \qquad \text{Scheme A}$$

$$E + I \underset{k_{-1}}{\overset{k_1}{\rightleftharpoons}} E{\cdot}I \underset{k_{rev}}{\overset{k_{for}}{\rightleftharpoons}} EI^* \qquad \text{Scheme B}$$

2.6.4. Jump-dilution assay

The dissociation rate constant (k_{off}) was determined from the recovery of enzyme activity after dilution of the preincubated enzyme-inhibitor complex [61,62,88]. Briefly, 1 nM of the enzyme was preincubated with 2.5, 5, 50, or 500 nM inhibitor, which was determined in pilot runs to balance two opposing needs: increase [I] to approach maximal preincubation occupancy, yet limit [I] to preserve a sufficiently large signal window after dilution. For several very tight binders we therefore did not force full saturation, as using higher [I] compressed the dynamic range of the curve. After a 30 min preincubation at 37 °C, the mixture was diluted 100-fold into assay buffer containing 200 μM substrate C. Owing to its limited solubility, substrate C was dissolved and diluted in methanol, and the final methanol concentration in the reaction mixture was adjusted to 1 %. The reaction progress was monitored at 2.5-min intervals over a 10-h period. Blank values (reaction mixture without enzyme) were subtracted, and the data was fitted to the rate equation for slow-binding inhibition (Eq. (1)):

$$[P] = v_s t + \frac{v_i - v_s}{k_{off}}\left(1 - e^{-k_{off} t}\right) \tag{1}$$

where [P] is the accumulated product concentration, v_i and v_s are the initial and steady-state reaction rates, t is the time, and k_{off} is the first-order dissociation rate constant for the conversion between v_i and v_s, representative for enzyme-inhibitor complex dissociation [73]. Under these conditions, rebinding is negligible [73]. For Scheme A, the observed recovery rate equals the dissociation constant (k_{off}). For Scheme B, the observed rate constant k_{off} is governed by the rate-limiting first-order step, and most likely reflects k_{rev}.

To avoid bias from the long linear tail in some curves, which adds many near-redundant points and can down-weight curvature, we fit only the informative, curved portion of the curve. For this, the raw data was provisionally fit to Eq. (1). From this fit, we evaluated the analytic derivative and scanned the time series with a rolling 10-point window. The onset of linearity t_{lin} was regarded as the time point where steady-state activity was reached, and was defined as the earliest index j at which the relative change satisfied:

$$\frac{\left|\frac{dP}{dt}(t_j) - \frac{dP}{dt}(t_{j-10})\right|}{\left|\frac{dP}{dt}(t_{j-10})\right|} \leq 1\% \tag{2}$$

Data up to t_{lin} were then refit to Eq. (1), and the resulting k_{off} was taken as the final estimate. An illustrative example is provided in Figure S10 and Figure S11. If curvature resolved faster than our sampling permitted (i.e., steady state reached before the earliest measurable points), we conservatively assigned k_{off} to $\geq 0.0016\ s^{-1}$, just above the highest resolvable rate measured in this study. Finally, the residence time (τ) is calculated as the reciprocal of the dissociation rate constant, i.e., $\tau = 1/k_{off}$. All calculations were automated using Python SciPy (version 1.10.1) and pandas (version 2.2.2) packages.

2.6.5. Data analysis

For each FAPI, three independent replicate estimates of k_{off} were obtained by jump-dilution assay (n = 3). The point estimate reported in tables is the sample mean $\overline{k}_{off}$, and residence time was summarized as $\hat{\tau} = 1/\overline{k}_{off}$. To quantify uncertainty around this mean, 95 % confidence intervals (CIs) were generated for $\overline{k}_{off}$ using a non-parametric bias-corrected and accelerated (BCa) bootstrap with B = 10,000 resamples. In each bootstrap sample, the *n* replicate values were resampled with replacement and the sample mean was computed; the BCa adjustment used jackknife estimates to compute the bias-correction (z_0) [89]. Confidence intervals for residence time were obtained by monotone transformation of the k_{off} bounds, reflecting $\tau = 1/k_{off}$. Because of the skewness of rate estimates and the non-linear transform, τ intervals are not symmetric around $\hat{\tau}$. Compounds with $n < 3$ replicates were reported without CIs. As a robustness check, we repeated the bootstrap on log k_{off} (variance-stabilizing scale) and back-transformed the resulting BCa bounds; results were similar.

2.6.6. Progress curve assay

Progress curve assays were performed to determine the association rate constant (k_{on}) and inhibition constant K_i. Due to the poor solubility

of substrate A (ZGP-AMC), we used substrate B (Table S3), at a final concentration of 35.8 μM, corresponding to 1.9x K_m. For each inhibitor, seven concentrations were selected based on preliminary experiments performed to identify the assay's effective measurement range. Inhibitor concentrations that were too high resulted in inhibition occurring within seconds, while those that were too low produced barely measurable inhibition even after several hours. For this assay, inhibitor was mixed with substrate and prewarmed at 37 °C in a 96-well plate. The reaction was initiated by adding FAP in a final concentration of 0.01 nM, and the AMC product formation was monitored for at least 2 h and up to 10 h for the slowest-binding inhibitors. Blank values (substrate without enzyme) were subtracted from the data, and the progress curves were fitted to the rate equation for slow binding inhibition (Eq. (3)):

$$[P] = v_s t + \frac{v_i - v_s}{k_{obs}}\left(1 - e^{-k_{obs}{}^* t}\right) \tag{3}$$

In this equation, [P], v_i, v_s and t are defined as described before, and k_{obs} is the observed pseudo-first-order rate constant for reaching steady-state velocity. To objectively define the dynamic range of the curve, i.e. the time required for the reaction to reach steady state,we computed the derivative of the fitted progress curve (see Fig. S10; Fig. S11). The dynamic range was defined as the time point at which the rate of change decreased to within 1 % of the value recorded 10 time points earlier (Eq. (2)). All calculations were executed using Python SciPy (version 1.10.1) and pandas (version 2.2.2) packages.

2.6.7. Calculation of association rate constant k_{on}

The association constant k_{on} for a slow-binding inhibitor could be derived by plotting the apparent pseudo-first-order rate constant k_{obs} against total inhibitor concentration ($[I]_0$). Depending on the inhibition mechanism, the resulting plot can be linear (indicative of the direct binding model, Scheme A) or hyperbolic (indicative of the two-step model, scheme B). In the experiments, most inhibitors conformed to the direct binding model (Scheme A), as evidenced by linear k_{obs} vs $[I]_0$ relationships. The data was fitted to Eq. (4):

$$k_{obs} = k_{off} + k_{on,app}\,[I]_0 \tag{4}$$

Where k_{obs} and k_{off} are defined as described before, $k_{on,app}$ is the apparent second order association rate constant, and $[I]_0$ is the total inhibitor concentration. A minority of inhibitors obeyed to the two-step model (Scheme B), characterized by the hyperbolic k_{obs} vs $[I]_0$ plots, and could be fitted via Eq. (5):

$$k_{obs} = k_{rev} + k_{for}\,\frac{[I]_0}{[I]_0 + K_{1,app}} \tag{5}$$

$$k_{on,app} = \frac{k_{for}}{K_{1,app}} \tag{6}$$

Where k_{obs} and $k_{on,app}$ are defined as described before, k_{for} is the forward first order rate constant of the second step, k_{rev} the reverse first order rate constant of the second step, $K_{1,app}$ the dissociation equilibrium constant of the initial complex (k_{-1}/k_1), and $[I]_0$ the total inhibitor concentration (see Table 6). For FAPIs conforming to the two-step model, $k_{on,app}$ was obtained using Eq. (6) and these entries were flagged in Table 7. In cases where $k_{obs}/[I]$ plots were concave (Table S6: **5**, **6**, **8**, **32**), k_{on} was estimated from the slope of the approximately linear region at the highest inhibitor concentrations. This approach reflects the fact that at high [I], the observed rate constant approaches pseudo-first-order behavior, and the slope of this region provides the best approximation of the true second-order k_{on}.

Then, after plotting to either model, the true association constant k_{on} was then calculated by correcting $k_{on,app}$ for substrate competition via Eq. (7):

$$k_{on} = k_{on,app}{}^*\left(1 + \left(\frac{S}{K_m}\right)\right) \tag{7}$$

Where $k_{on,app}$ and S are defined as described before and K_m is the Michaelis-Menten constant for substrate B. For all obtained k_{on} values, the 95 % CI was calculated on at least 3 replicates. In cases where association was too rapid to extract a reliable k_{obs} from the progress curves, even at inhibitor concentrations as low as 0.1 nM, we conservatively reported k_{on} as $\geq 5 \times 10^6\ M^{-1}\ s^{-1}$, corresponding to just above the fastest measurable rate.

Although in principle k_{off} can be obtained from the y-intercept of a k_{obs} versus $[I]_0$ plot (as described in Eq. (4)) and in many cases agreed with JDA measurements, the extremely slow off-rates of some inhibitors yielded intercepts clustered at or even below zero. Consequently, we did not rely on this method for k_{off} estimation.

2.6.8. Calculation of inhibition constant K_i

In tight-binding scenarios – where the total inhibitor concentration is comparable to the enzyme concentration and a significant fraction of inhibitor is sequestered in the enzyme-inhibitor complex – the classical assumption that $[I] = [I]_0$ no longer applies. Therefore, we employed the Morrison equation (Eq. (8)) to account explicitly for inhibitor depletion and accurately calculate K_i values under these conditions, using the raw data from the progress curve assay as input:

$$v_s = v_0{}^*\left(1 - \frac{(E_0 + I_0 + K_{i,app}) - \sqrt{(E_0 + I_0 + K_{i,app})^2 - 4E_0 I_0}}{2E_0}\right) \tag{8}$$

In this expression, v_0 and v_s represent the steady-state reaction velocities in the absence and presence of inhibitor (I) respectively, $K_{i,app}$ is the apparent inhibition constant and E_0 is the active enzyme concentration in the reaction medium (0.01 nM). The true inhibition constant K_i was then calculated by correcting $K_{i,app}$ for substrate competition using Eq. (9):

$$K_{i,app} = K_i{}^*\left(1 + \left(\frac{S}{K_m}\right)\right) \tag{9}$$

For comparison, we also calculated K_i with the obtained k_{off} and k_{on} values from the JDA and progress curve via Eq. (10):

$$K_i = \frac{k_{off}}{k_{on}} \tag{10}$$

2.7. Grating-coupled interferometry

Binding kinetics were also measured for reference FAPIs **UAMC-1110** and **6d,** and FAPI **17** using a grating-coupled interferometry system (Creoptix® WAVE, Creoptix® AG). Experiments were performed at 25 °C using quasi-planar 4PCP-NTA sensor chips. The chip surface is coated with a polyethylene glycol-carboxyl (PCP) polymer, functionalized with nitrilotriacetic acid (NTA), which provides a low-fouling background to minimize non-specific interactions. FAP was buffer-exchanged to capture buffer (25 mM MES, 100 mM NaCl, pH 6) and immobilized on the sensor surface via His-tag capture in the same buffer, followed by amine coupling and subsequent Ni-stripping using EDTA, achieving an immobilization level of approximately 1500 pg/mm^2 (Amine coupling kit AN (NHS) Xantec®). The reference channel was subjected to the same immobilization procedure but without ligand. FAPIs were dissolved in DMSO to prepare 1 mM stock solutions and further diluted in running buffer (25 mM Tris, 150 mM NaCl, 0.05 % Tween 20, pH 7.4). FAPIs were injected in a series of five increasing concentrations (**UAMC-1110** and **6d:** 125 pM–2 nM; **17:** 4.7–150 nM) in running buffer at a constant flow rate (150 μL/min) and injection duration (160 s). The dissociation phase between concentrations was 45 s, and an extended dissociation phase of 600 s for the highest

concentration. To account for bulk refractive index effects, a DMSO calibration curve was generated by injecting a series of DMSO concentrations (0.19 %–0.75 % v/v) in running buffer. During kinetic analysis, sensorgrams were solvent-corrected with this curve and double-referenced by subtracting reference channel and buffer blank signals. Kinetic parameters (association rate constant k_{on}, dissociation rate constant k_{off}, and dissociation constant K_D) were determined by global fitting of the data to a 1:1 binding mass transfer model using the instrument's analysis software (WAVEcontrol, Creoptix® AG). All experiments were performed in at least triplicate to ensure reproducibility, and error values represent standard deviations.

2.8. Surface-plasmon resonance

rhFAP was buffer-exchanged to capture buffer (25 mM MES, 100 mM NaCl, pH 6) and immobilized using amine coupling on a CM5 chip in a Biacore T100 device in the same buffer. Kinetic measurements were performed by injecting increasing concentrations of UAMC-1110 (125 pM - 2 nM) in running buffer (10 mM HEPES, 150 mM NaCl, 3.4 mM EDTA, 0.005 % Tween 20, pH 7.4), using the following experimental parameters: flow rate of 30 µl/min, injection duration of 240 s, intermediate dissociation of 85 s and final dissociation of 600 s. Fitting was performed using the Biacore T200 Evaluation software and the 1:1 binding model.

2.9. Covalent docking

2.9.1. Crystal structure selection

Two crystal structures of FAP were available: one containing the non-covalently bound ligand **linagliptin** (PDB: 6Y0F), and the other representing the apo structure (PDB: 1Z68) [81,90]. Two key differences in the active site were identified between the crystal structures (Fig. S12). First, Y541 is positioned closer to the catalytic triad in the apo structure, preventing the interaction between H734 and the oxyanion forming on the α-ketoamide warhead. By contrast, the co-crystallized structure allows greater conformational flexibility for the aromatic moieties attached to the α-ketoamide warhead. The second difference lies in the orientation of F350. In the apo structure, F350 could form a π-π stacking interaction with the quinolinone moiety of the FAPIs [75]. Therefore, the crystal structure with **linagliptin** (PDB: 6Y0F) was selected, and the sidechain dihedral angles of F350 were manually adjusted to match those in the apo structure.

2.9.2. System preparation

Initially, chains C and D were retained, and all other atoms were removed using PyMOL version 2.4.1. Missing residues were modeled using ModLoop, and the most favorable side chain conformations were selected via MolProbity [91,92]. As a result, the following residues were flipped: N60, Q167, N169, N413, H477, N491, N500, N733 and N742. The protonation states of the residues were predicted using H++ (version 4.0) and PROPKA 3 [93,94]. In the H++ calculations, a pH value of 6.3 was specified [95]. Buried and surface residues were evaluated by varying the internal dielectric between 4 and 10, and the salinity and external dielectric were kept at 0.15 and 80, respectively. Four cysteine bridges were identified: C321–C332, C438–C441, C448–C466 and C643–C755. Histidine residues were either protonated at the delta (H378, H442, H477, H734 and H750) or epsilon nitrogen atom (H69, H338, H376, H676, H698, H706, H743 and H747). One aspartate residue was protonated (D228), given the predicted pKa was 6.7 and 6.8 as calculated by H++ and PROPKA 3, respectively. Protonation states of the ligands were computed using Jaguar pKa module in Schrödinger (version 14.2.118) [96–98]. The predicted pKa of the piperazine nitrogen adjacent to the propoxy linker was 6.46, indicating a slightly higher likelihood of protonation under mildly acidic tumor microenvironmental conditions (pH 6.3).

2.9.3. Covalent docking

The covalent docking simulations were executed using Maestro [99]. The catalytic S624 was specified as the reactive residue. The centroid of **vildagliptin** (PDB: 3W2T), a covalent inhibitor bound to DPP4 containing a nitrile warhead, was selected as the box center in the initial docking of **5** and **UAMC-1110** [100]. For the remaining compounds, the centroid of covalently docked **5** was defined as the box center. The reaction type for most compounds was specified as nucleophilic addition to a double bond. The SMARTS pattern was adjusted to specify the α-ketoamide moiety, and the correct electrophilic carbon atom. The reaction type for **UAMC-1110** was set to triple bond. The pose prediction docking mode was applied with an output of twenty-five poses per ligand reaction site and all other parameters were kept at their default values. The most probable binding poses were selected based on two criteria: (1) the alignment of the pyrrolidine ring with that of **vildagliptin** in the DPP4-bound crystal structure (PDB: 3W2T), and (2) the orientation of the formed hydroxyl group toward H734. Lastly, the top-ranked binding poses were compared and manually refined to ensure favorable protein–ligand interactions.

3. Results

3.1. High-quality rhFAP ensures accurate kinetic analyses

Accurate measurement of kinetic parameters (k_{on}, k_{off}, and K_i) requires a highly pure, active, and stable enzyme preparation. We therefore expressed the human FAP ectodomain (residues 26–760) in Freestyle™ 293-F cells and purified it to $\geq$ 99 % homogeneity (Fig. S13A–B). SDS-PAGE analysis revealed a prominent band at 90 kDa, the FAP monomer, and a secondary band around 180 kDa (Fig. S13C). Mass spectrometry verified both as FAP (Table S1; Table S2), resulting in an excellent sample purity. The process consistently yielded around 1.5 mg FAP per liter of Freestyle™ 293-F cell culture and a specific endopeptidase activity of 5900 U/g and could be stored for up to one month at 4 °C (data not shown). Michaelis-Menten parameters were determined for substrate B (K_m: 19 ± 2 µM; k_{cat}: 35 ± 1 s^{-1}) and substrate C (K_m: 77 ± 14 µM; k_{cat}: 6.7 ± 0.5 s^{-1}) (Table S3, Figure S14 and 15).

Proper N-glycosylation was verified by PNGase F digestion, which produced a slightly larger molecular-weight shift for the rhFAP from mammalian HEK293-F cells compared with earlier produced rhFAP from insect Sf9 cells (produced as described earlier [31]) (Fig. S16). Active-site titration demonstrated that virtually 100 % of the rhFAP is catalytically active, considering 0.968–1.087 nM measured vs 1 nM theoretical rhFAP; Fig. S17). Differential scanning fluorimetry showed maximum thermal stability (65 ± 0.5 °C) of rhFAP at pH 5–6, with a melting temperature of 61 ± 0.5 °C for a buffer similar to our standard assay buffer (pH 8, 140 mM NaCl), which was well above the assay temperature (37 °C) (Fig. S18). NaCl concentration only had a minor effect on stability. Together, these characteristics – purity, glycosylation, functional active-sites, and thermal resilience – provide a robust foundation for all downstream kinetic assays.

3.2. Enzyme concentration biases IC_{50} of tight-binding inhibitors

Half-maximal inhibitory concentration (IC_{50}) assays fail to report true affinity for tight-binding inhibitors because the apparent IC_{50} shifts with enzyme concentration. Indeed, increasing [FAP] from 0.1 to 2.7 nM caused a corresponding rise in IC_{50} (Fig. 1; Table S4) for **UAMC-1110** and FAPI 1 (Table 1), demonstrating that conventional IC_{50} measurements cannot discriminate high-affinity inhibitors under tight-binding conditions. Moreover, IC_{50} ignores the kinetic dimensions of binding and is therefore ill-suited to identify candidates with prolonged target residence times (i.e., low k_{off} values).

To address this limitation, we implemented jump-dilution assays (JDAs) and progress curve assays to obtain direct estimates of the dissociation rate constant (k_{off}) and association rate constant (k_{on}).

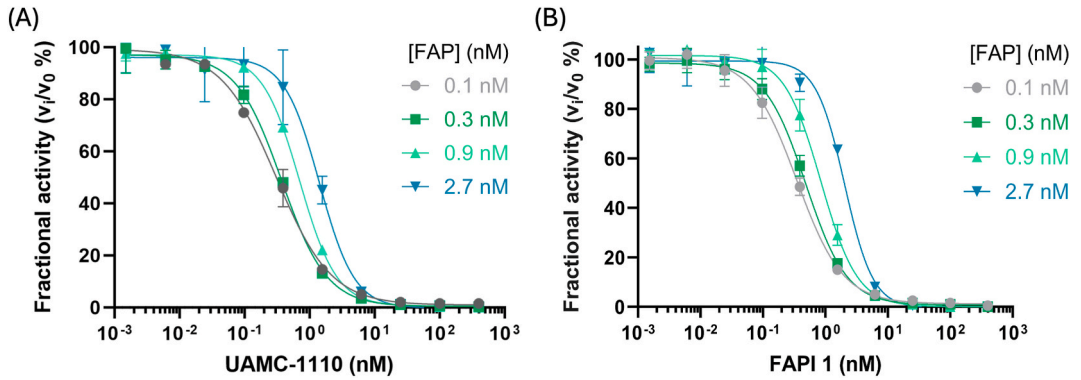

Fig. 1. IC_{50} values of the tight-binding inhibitors **UAMC-1110** and FAPI 1 increase with rising enzyme concentration. (**A**) Dose-response curves for **UAMC-1110** against rhFAP at increasing enzyme concentrations (0.1, 0.3, 0.9, and 2.7 nM). (**B**) Dose-response curves for FAPI 1 against rhFAP at increasing enzyme concentrations (0.1, 0.3, 0.9, and 2.7 nM). Enzyme activity is expressed as fractional activity (v_i/v_0), where v_i and v_0 represent the initial reaction velocity in the presence and absence of inhibitor, respectively. Increasing rhFAP concentrations cause a shift in the inhibition curves, consistent with tight-binding kinetics.

Table 1
Residence times ($\tau = 1/k_{off}$) from jump-dilution for matched FAPI scaffolds differing in warhead chemistry. Point estimates are computed as $\hat{\tau} = 1/\bar{k}_{off}$ from n = 3 independent replicates per compound. 95 % confidence intervals (CI) were obtained via non-parametric bootstrapping on k_{off}.

Structure	FAPI	R	τ (h)	95 % CI (h)
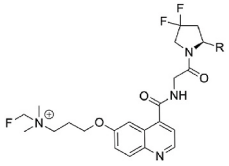	1	⁻CN	0.47	0.44–0.50
	2	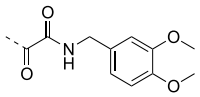	5.4	5.3–5.4
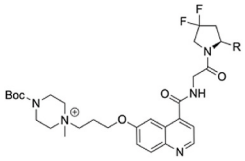	3	⁻CN	0.74	0.69–0.80
	4	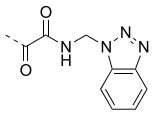	1.9	1.8–2.0

These kinetic measurements offer a more comprehensive evaluation of inhibitor efficacy than IC_{50} or K_i alone, and they are better suited for selecting the most promising FAP-inhibitors (FAPIs) for *in vivo* research, while retaining medium-throughput characteristics.

3.3. The jump-dilution assay is well-suited for estimating the FAPI-target residence time

To validate the JDA and establish suitable testing conditions, we selected two structurally distinct reference FAPIs: **UAMC-1110,** and compound **6d** from Šimková et al. [75]. Repeatability was confirmed by two independent runs per compound on the same day, which yielded statistically insignificant differences in k_{off} ($p > 0.05$; one-way ANOVA). Intermediate precision, assessed across three consecutive days and by three operators, likewise showed no significant day-to-day or operator-to-operator variation ($p > 0.05$; two-way ANOVA). Robustness testing at 25 °C vs 37 °C and using preincubation times of 15, 30, and 60 min likewise produced consistent k_{off} values ($p > 0.05$; one-way ANOVA). Together, these data confirm that our JDA protocol delivers reproducible dissociation kinetics (Fig. S19).

Next, we benchmarked the k_{off} estimates from JDA against real-time interaction analysis via grating-coupled interferometry (GCI) and surface-plasmon resonance (SPR) (Figs. S20–S23). **UAMC-1110** exhibited a $0.47 \pm 0.10 \times 10^{-3}$ s^{-1} k_{off} using GCI and a $1.3 \pm 0.5 \times 10^{-3}$ s^{-1} k_{off} using SPR, vs a $1.6 \pm 0.1 \times 10^{-3}$ s^{-1} k_{off} using JDA, reflecting a slight overestimation of the JDA for this fast-dissociating ligand compared with GCI but a strong correlation with the k_{off} obtained via SPR (n = 3). Another literature FAPI, **Šimková et al. compound 6d** [75] showed excellent concordance: $0.18 \pm 0.05 \times 10^{-3}$ s^{-1} (n = 3) k_{off} by GCI versus a $0.16 \pm 0.01 \times 10^{-3}$ s^{-1} k_{off} by JDA (n = 3; not measured by SPR). A third FAPI used for validation (**17**) demonstrated a $0.19 \pm 0.03 \times 10^{-3}$ s^{-1} (n = 3) k_{off} by GCI versus a $0.15 \pm 0.02 \times 10^{-3}$ s^{-1} k_{off} by JDA (n = 3). These results indicate that the JDA is well-suited to estimate k_{off} for FAPIs while offering higher throughput, making it ideal for broad k_{off} screening.

Next, we investigated several clinically used reference FAPIs. The peptide-based tracer **FAP-2286** ($\pm^{nat}$Lu) dissociated too rapidly from FAP to quantify k_{off} by JDA [55,101]. The carbonitrile tracer **FAPI-74**, which carries a bulky chelator on the quinoline C6 side chain, exhibited a $1.1 \pm 0.2 \times 10^{-3}$ s^{-1} k_{off} (n = 3) [78]. By contrast, the dimeric carbonitrile-warhead reference FAPIs [34] exhibited a very low $0.051 \pm 0.008 \times 10^{-3}$ s^{-1} k_{off} for **[^{nat}Lu] Lu-DOTAGA.Glu.(FAPi)$_2$** and a $0.045 \pm 0.002 \times 10^{-3}$ s^{-1} k_{off} for the corresponding metal-free **DOTAGA.Glu.(FAPi)$_2$** ligand (n = 3). A k_{off} value of $0.12 \pm 0.02 \times 10^{-3}$ s^{-1} was observed for FAPI-mFS, reflecting a moderately low off rate.

3.4. α-Ketoamide FAPIs exhibit longer residence times than carbonitriles

We evaluated the dissociation kinetics of 35 in-house developed FAPIs, differing in warhead chemistry and substituents, the position and functionalization of the quinoline side chain, the dipeptide core motif, and pyrrolidine fluorination (Tables 1–5; Table S5). All kinetic SAR data are shown as τ to facilitate intuitive comparison ($\tau = 1/k_{off}$) rather than the raw rate constants, which are provided in Table 7. First, we assessed

Table 2
Residence times of FAPIs bearing α-ketoamide warheads with diverse substituents: dimethoxybenzyl (**11**), benzotriazolyl (**13**, **14**), diethoxyphosphoryl (**17**, **22**), benzodioxolyl (**24**, **25**), difluoromethoxyphenyl (**26**, **27**), tetrahydrofuranyl (**28**, **29**) and oxazolyl (**30**). Point estimates are computed as $\hat{\tau} = 1/\bar{k}_{off}$ from n = 3 independent replicates per compound. 95 % confidence intervals (CI) were obtained via non-parametric bootstrapping on k_{off}.

Structure	FAPI	R	τ (h)	95 % CI (h)
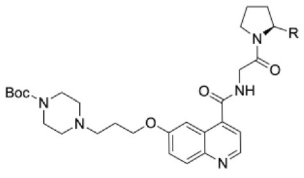	5	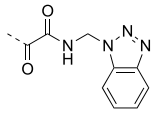	5.6	4.7–6.4
	6	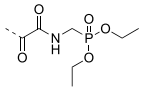	3.2	2.3–4.1
	7	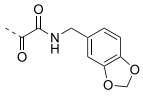	1.8	1.5–2.1
	8	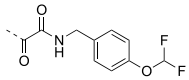	2.5	2.3–3.2
	9	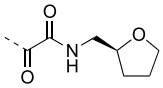	6.6	6.0–7.4
	10	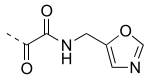	0.69	0.62–0.78
	11	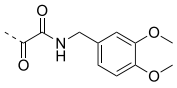	3.4	3.4–3.4
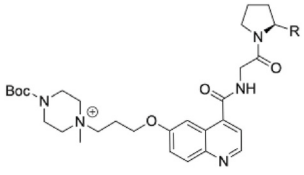	12	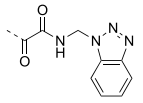	12	11–13
	13	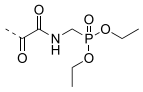	1.1	1.0–1.2
	14	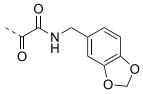	2.2	2.0–2.5
	15	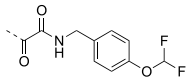	2.2	2.0–2.5
	16	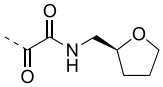	0.26	0.25–0.26

the impact of warhead type by comparing two matching FAPI scaffolds bearing either a carbonitrile (**1**, τ = 0.47 h; **3**, τ = 0.74 h) or an α-ketoamide warhead (**2**, τ = 5.4 h; **4**, τ = 1.9 h), which indicated that α-ketoamides generally extend binding lifetimes, by up to an order of magnitude (Table 1).

We next examined how α-ketoamide substituents modulate τ relative to the literature dimethoxyphenyl reference [75] (**5**; τ = 5.6 h) on two matching scaffolds (quinoline C6 side chain: tertiary amine vs quaternary-ammonium; Table 2). On the tertiary-amine backbone, benzotriazolyl (**6**; τ = 3.2 h), diethoxyphosphoryl (**7**; τ = 1.8 h), benzodioxolyl (**8**; τ = 2.5 h) and oxazolyl (**11**; τ = 3.4 h) substituents shortened τ, while the difluoromethoxyphenyl substituent (**9**; τ = 6.6 h) modestly extended τ versus reference [75]. In contrast, on the quaternary-ammonium scaffold, the benzotriazolyl substituent delivered the longest τ (**12**; τ = 12.0 h), whereas diethoxyphosphoryl (**13**; τ = 1.1 h), benzodioxolyl (**14**; τ = 2.2 h) and difluoromethoxyphenyl (**15**; τ = 2.2 h) substituents all produced substantially shorter τ. Across both scaffolds, the tetrahydrofuranyl substituent (**10**, **16**; τ = 0.26–0.69 h) resulted in the lowest τ, indicating that this moiety poorly stabilizes the tetrahedral intermediate.

Looking at the effect of quinoline C6 substitution specifically, a small aliphatic side chain such as triethylammoniopropyl (**17**; τ = 1.8 h)

Table 3
Residence times ($\tau = 1/k_{off}$) of FAPIs, comparing carbonitrile and α-ketoamide warheads across varied quinoline substitution and side-chain modifications. Both warhead series include analogues with an unsubstituted quinoline or a 6-substituted quinoline bearing linkers of different lengths, steric bulk, and polarity; α-ketoamide FAPIs additionally feature quinoline-8 substituents. Point estimates are computed as $\hat{\tau} = 1/\bar{k}_{off}$ from n = 3 independent replicates per compound. 95 % confidence intervals (CI) were obtained via non-parametric bootstrapping on k_{off}.

	FAPI	R_1	R_2	τ (h)	95 % CI (h)
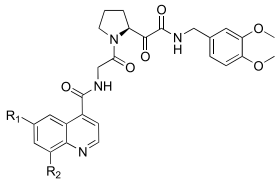	17	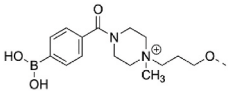	H	1.8	1.6–2.0
	18	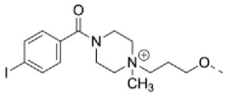	H	4.1	3.9–4.3
	19	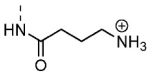	H	7.2	6.0–8.3
	20	H	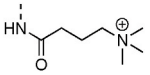	0.52	0.49–0.58
	21	H	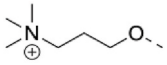	0.47	0.39–0.54
	Šimková et al. 6d [75]	H	H	1.8	1.6–1.8
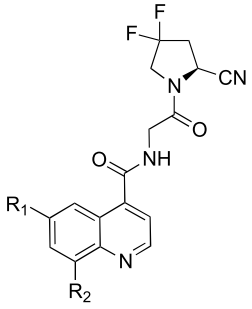	1	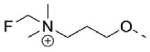	H	0.47	0.44–0.50
	22	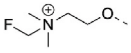	H	0.44	0.41–0.47
	23	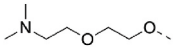	H	0.50	0.44–0.59
	24	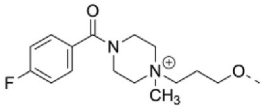	H	0.55	0.49–0.69
	25	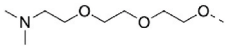	H	1.1	1.0–1.2
	26	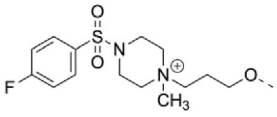	H	0.99	0.93–1.09
	27	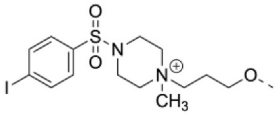	H	0.94	0.91–0.96
	28	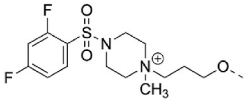	H	1.2	1.1–1.2
	UAMC-1110	H	H	0.17	0.16–0.18
FAPI-74				0.26	0.23–0.33
$DOTAGA.Glu.(FAPi)_2$				6.2	6.1–6.3
$[^{nat}Lu]Lu\text{-}DOTAGA.Glu.(FAPi)_2$				5.5	4.8–6.6

Within α-ketoamide scaffolds bearing a propoxy linker at quinoline C6, a quaternary ammonium outperformed a tertiary amine at the distal end of the propoxy linker (**17** → **29**; 1.8 → 1.7 h, and **30** → **31**; 6.6 → 5.0 h). Regarding pyrrolidine C2 fluorination, in the benzotriazolyl series, introducing two fluorines reduced residence time (**4**; τ = 1.9 h) compared with the non-fluorinated analogue (**12**; τ = 12 h) (Table 4). By contrast, in FAPIs with a dimethoxybenzyl-substituted α-ketoamide warhead, fluorination consistently prolonged τ across different backbones: **5** → **32**; 5.6 → 7.2 h, **17** → **30**; 1.8 → 6.6 h, and **29** → **31**; 1.7 → 5.0 h.

Table 4
Residence times ($\tau = 1/k_{off}$) of α-ketoamide FAPIs comparing tertiary versus quaternary amine substituents in the quinoline-6 side chain, and the presence or absence of pyrrolidine C2 fluorination. Point estimates are computed as $\hat{\tau} = 1/\bar{k}_{off}$ from n = 3 independent replicates per compound. 95 % confidence intervals (CI) were obtained via non-parametric bootstrapping on k_{off}.

Structure	FAPI	R	X	τ (h)	95 % CI (h)
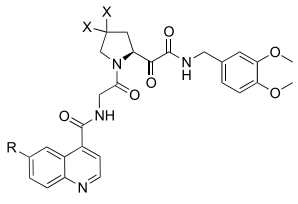	5	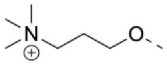	H	5.6	4.7–6.4
	17	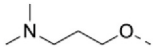	H	1.8	1.6–2.0
	29	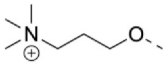	H	1.7	1.5–1.9
	30	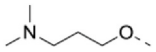	F	6.6	6.0–7.8
	31	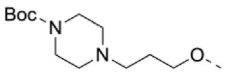	F	5.0	4.8–5.3
	32	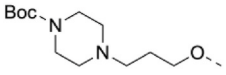	F	7.2	5.6–9.7
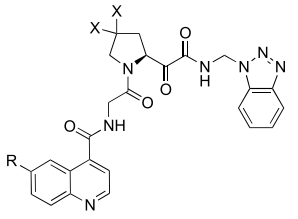	4	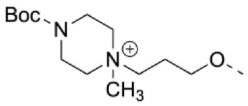	F	1.9	1.8–2.0
	12	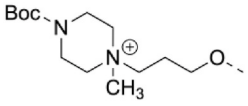	H	12	11–13

Table 5
Residence times of α-ketoamide FAPIs bearing Gly-Pro versus D-Ala-Pro dipeptide motifs, highlighting how P2 backbone stereochemistry influences inhibitor dissociation kinetics. Point estimates are computed as $\hat{\tau} = 1/\bar{k}_{off}$ from n = 3 independent replicates per compound. 95 % confidence intervals (CI) were obtained via non-parametric bootstrapping on k_{off}.

Structure	FAPI	R	τ (h)	95 % CI (h)
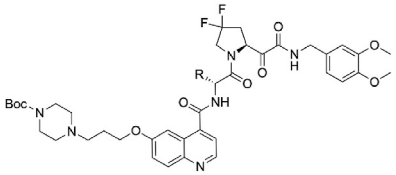	32	H	7.2	5.6–9.7
	33	CH_3	4.4	4.3–4.6

The chelator-containing analogues **34** (DOTA) and **35** ([^{nat}Lu]Lu-DOTA) displayed similar residence times, with τ values of 3.7 h and 4.7 h, respectively, and overlapping 95 % confidence intervals (3.1–4.3 h and 3.8–5.6 h) (Table 6). The same pattern was observed for the dimeric structures **DOTAGA.Glu.(FAPi)$_2$** and **[^{nat}Lu] Lu-DOTAGA.Glu.(FAPi)$_2$**, which showed τ values of 6.2 h and 5.5 h, respectively, also with overlapping confidence intervals.

Table 6
Residence times of α-ketoamide FAPIs bearing a DOTA(GA) chelator with or without ^{nat}Lu. Point estimates are computed as $\hat{\tau} = 1/\bar{k}off$ from n = 3 independent replicates per compound. 95 % confidence intervals (CI) were obtained via non-parametric bootstrapping on k_{off}.

Structure	FAPI	R_1	τ (h)	95 % CI (h)
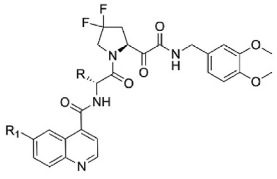	34	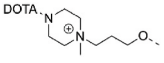	3.7	3.1–4.3
	35	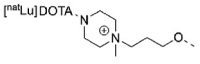	4.7	3.8–5.6
DOTAGA.Glu.(FAPi)$_2$			6.2	6.1–6.3
[^{nat}Lu]Lu-DOTAGA.Glu.(FAPi)$_2$			5.5	4.8–6.6

Table 7
Rate and equilibrium constants. Dissociation rate constants (k_{off}, 10^{-3} s^{-1}) were measured by jump-dilution assays, and association rate constants (k_{on}, 10^6 M^{-1} s^{-1}) were obtained from progress curve assays. Equilibrium inhibition constants (K_i) are reported both as the ratio k_{off}/k_{on} (column "K_i (k_{off}/k_{on})") and as derived from Morrison equation fits to the progress curves (column "K_i (Morrison)"). Unmeasurable k_{off} values were conservatively set to $\geq 1.6 \times 10^{-3}$ s^{-1} (just above the highest resolvable rate), and unmeasurable k_{on} values were set to $\geq 5 \times 10^6$ M^{-1} s^{-1} (just above the fastest measurable rate). Missing Morrison values ("/") indicate cases where binding was too rapid to allow reliable fitting. Values are means ± SEM from n = 3 independent experiments. *association rate constant derived from the two-step model. ND, not determined.

FAPI	k_{off} (10^{-3} s^{-1}) (Jump-dilution)	k_{on} (10^6 M^{-1} s^{-1}) (Progress curve)	K_i (k_{off}/k_{on}) (nM)	K_i (Morrison) (nM)
1	0.59 ± 0.03	0.24 ± 0.04	2.5	1.9
2	0.052 ± 0.001	0.049 ± 0.004	1.1	0.74
3	0.38 ± 0.02	0.53 ± 0.07	0.72	0.57
4	0.14 ± 0.01	0.11 ± 0.01	1.3	0.10
5	0.049 ± 0.005	0.31 ± 0.08	0.16	0.035
6	0.086 ± 0.018	0.48 ± 0.15	0.18	0.058
7	0.15 ± 0.02	0.23 ± 0.02	0.65	0.91
8	0.11 ± 0.01	0.37 ± 0.05	0.30	0.26
9	0.042 ± 0.01	0.45 ± 0.05	0.093	0.12
10*	0.40 ± 0.03	0.72 ± 0.30	0.55	0.36
11	0.082 ± 0.001	0.51 ± 0.05	0.16	0.33
12	0.023 ± 0.001	0.13 ± 0.01	0.18	0.012
13	0.25 ± 0.01	0.25 ± 0.04	1.0	0.62
14	0.13 ± 0.01	0.68 ± 0.08	0.19	0.24
15	0.13 ± 0.01	0.53 ± 0.03	0.24	0.28
16*	1.1 ± 0.1	1.9 ± 1.4	0.58	2.3
17*	0.15 ± 0.02	0.080 ± 0.009	1.9	1.1
18*	0.069 ± 0.004	0.45 ± 0.15	0.15	0.31
19	0.039 ± 0.005	0.98 ± 0.11	0.040	0.014
20	0.53 ± 0.04	1.2 ± 0.3	0.44	0.90
21*	0.59 ± 0.07	1.7 ± 0.2	0.35	1.3
22	0.63 ± 0.03	0.064 ± 0.007	9.8	6.4
23	0.55 ± 0.06	0.20 ± 0.02	2.7	2.1
24	0.50 ± 0.06	0.37 ± 0.06	1.4	0.52
25	0.25 ± 0.02	0.52 ± 0.11	0.48	0.18
26	0.28 ± 0.02	2.2 ± 0.2	0.13	0.24
27	0.30 ± 0.01	3.2 ± 0.4	0.094	0.095
28	0.24 ± 0.01	3.6 ± 0.4	0.067	0.10
29	0.16 ± 0.01	0.066 ± 0.004	2.4	1.4
30	0.042 ± 0.004	0.040 ± 0.006	1.0	0.081
31	0.055 ± 0.003	0.045 ± 0.006	1.2	0.22
32	0.038 ± 0.007	0.26 ± 0.02	0.15	0.017
33	0.063 ± 0.002	0.10 ± 0.01	0.63	0.37
34	0.77 ± 0.13	ND	ND	ND
35	0.60 ± 0.10	ND	ND	ND
UAMC-1110	1.6 ± 0.1	1.7 ± 0.2	0.94	1.2
Šimková et al. [75] 6d	0.16 ± 0.01	0.78 ± 0.11	0.20	0.11
FAPI-74	1.1 ± 0.1	≥5	≤0.22	/
DOTAGA.Glu.$(FAPi)_2$	0.045 ± 0.002	2.7 ± 0.3	0.017	0.0042
[^{nat}Lu]Lu-DOTAGA.Glu.$(FAPi)_2$	0.051 ± 0.005	4.6 ± 0.5	0.011	0.0042
FAP-2286	≥1.6	≥5.0	0.32	/
[^{nat}Lu]Lu-FAP-2286	≥1.6	≥5.0	0.32	/
FAPI-mFS	0.12 ± 0.02	ND	ND	ND

produced no change compared with the unsubstituted reference (**Šimková et al. Compound 6d** [75], τ = 1.8 h) (Table 3). By contrast, carbonitrile FAPIs, characterized by a shorter τ as demonstrated above (baseline **UAMC-1110**; τ = 0.17 h), showed substantial gains with the introduction of a C6 substituent: a (fluoromethyl)dimethylammonioethane linker (**22**; τ = 0.44 h) more than doubled τ, but extending the alkyl spacer from two to three carbons (**1**; τ = 0.47 h) yielded only marginal further improvement. Substituting the alkyl spacer with a PEG_2 linker (**23**; τ = 0.50 h) and, more markedly, a PEG_3 linker (**25**; τ = 1.1 h) progressively slowed dissociation. In contrast, relocating the triethylammoniopropyl group from quinoline C6 (**17**; τ = 1.8 h) to C8, either as 4-aminobutanamide (**20**; τ = 0.52 h) or as triethylammoniobutanamide (**21**; τ = 0.47 h), reduced τ by 3–4 ×, underscoring steric or electrostatic penalties associated with the C8 position, although the substituents were not completely identical.

We then explored larger, aromatic substituents as side chains of the quinoline C6 to probe peripheral subsite engagement (Table 3). On α-ketoamide FAPIs, replacing the terminal amine of the short aliphatic C6 propoxy linker discussed before (**17**; τ = 1.8 h) with a phenylboronic-acid piperazinamide (**18**) raised τ to 4.1 h, and installing a iodobenzene piperazinamide (**19**) further extended τ to 7.2 h. In the carbonitrile series, characterized by a shorter baseline τ (baseline **UAMC-1110**; τ = 0.17 h), appending the same iodobenzene piperazinamide (**24**) also increased τ, to 0.55 h. Substituting the amide linker between rings for a sulphonamide linker (**26**) further improved τ to 0.99 h, indicating that the sulphonamide bond better positions the aryl moiety in the FAP pocket. Tuning of this piperazine-sulphonamide-aryl motif revealed that the *meta*-difluorophenyl derivative (**28**; τ = 1.2 h) exhibited a longer τ than both the mono-fluoro (**26**, τ = 0.99 h) and iodo (**27**, τ = 0.94 h) analogues. Yet, the dissociation rate of these monomeric analogues remained markedly faster than that of the dimeric FAPIs **[^{nat}Lu] Lu-DOTAGA.Glu.$(FAPi)_2$** (τ = 5.5 h) and the corresponding **DOTAGA.Glu.$(FAPi)_2$** (τ = 6.2 h).

Next, we also probed the influence of the amino acid backbone stereochemistry (Table 5). Replacing the widely adopted Gly-Pro motif (**32**; τ = 7.2) with its *D*-Ala-Pro analogue (**33**; τ = 4.4) reduced τ, confirming the importance of the stereochemistry at P2 when designing dipeptide-based inhibitors.

3.5. Positive correlation of k_{on} and k_{off} reveals kinetic trade-offs in FAPIs

Analysis of the progress curve data yielded association rate constants (k_{on}) and inhibition constants (K_i) for each FAPI (Table 7; Table S6). For carbonitrile FAPIs, k_{on} spanned nearly two orders of magnitude (6.4×10^4 M^{-1} s^{-1} for **22** to 3.6×10^6 M^{-1} s^{-1} for **28**). For α-ketoamide FAPIs, k_{on} likewise varied by ~ two orders of magnitude (4.0×10^4 M^{-1} s^{-1} for **30** to 1.9×10^6 M^{-1} s^{-1} for **16**). When looking into the carbonitrile FAPIs specifically, a K_i vs k_{on} correlation plot showed a logical inverse relationship (Fig. 2A), with faster associators tending to have tighter equilibrium affinities (slope, $\log_{10}$-$\log_{10} = -1.3$; 95 % CI -2.0 – 0.6; $R^2 = 0.64$). K_i vs k_{off} displayed a logical positive correlation (slope, $\log_{10}$-$\log_{10}$ = 2.1; 95 % CI 1.4–2.7; R^2 = 0.84; Fig. 2B). The two dimeric reference FAPIs **[^{nat}Lu] Lu-DOTAGA.Glu.$(FAPi)_2$** and **DOTAGA.Glu.$(FAPi)_2$** cluster at the lower-right of panel A (high k_{on}, low K_i) and the lower-left of panel B (low k_{off}, low K_i). When the two FAPI dimers were omitted from the regression analysis, because their avidity-driven binding is not directly comparable to monomeric ligands, the outcomes for both K_i vs k_{on} ($R^2 = 0.70$) and K_i vs k_{off} ($R^2 = 0.51$) remained similar. In contrast to the carbonitriles, the K_i vs k_{on} relation is essentially non-existing for the α-ketoamide FAPIs (slope, $\log_{10}$-$\log_{10} = 0.1$; 95 % CI -0.5 – 0.6; $R^2 = 0.01$; Fig. 2C). Varying k_{on} does not translate into systematic changes in K_i. However, K_i vs k_{off} displayed a clear positive correlation, similar to the carbonitriles, with an acceptable goodness of fit (slope, $\log_{10}$-$\log_{10}$ = 1.1; 95 % CI 0.7–1.6; R^2 = 0.55; Fig. 2D).

Plotting k_{off} against k_{on} on a log-log scale showed a weak positive

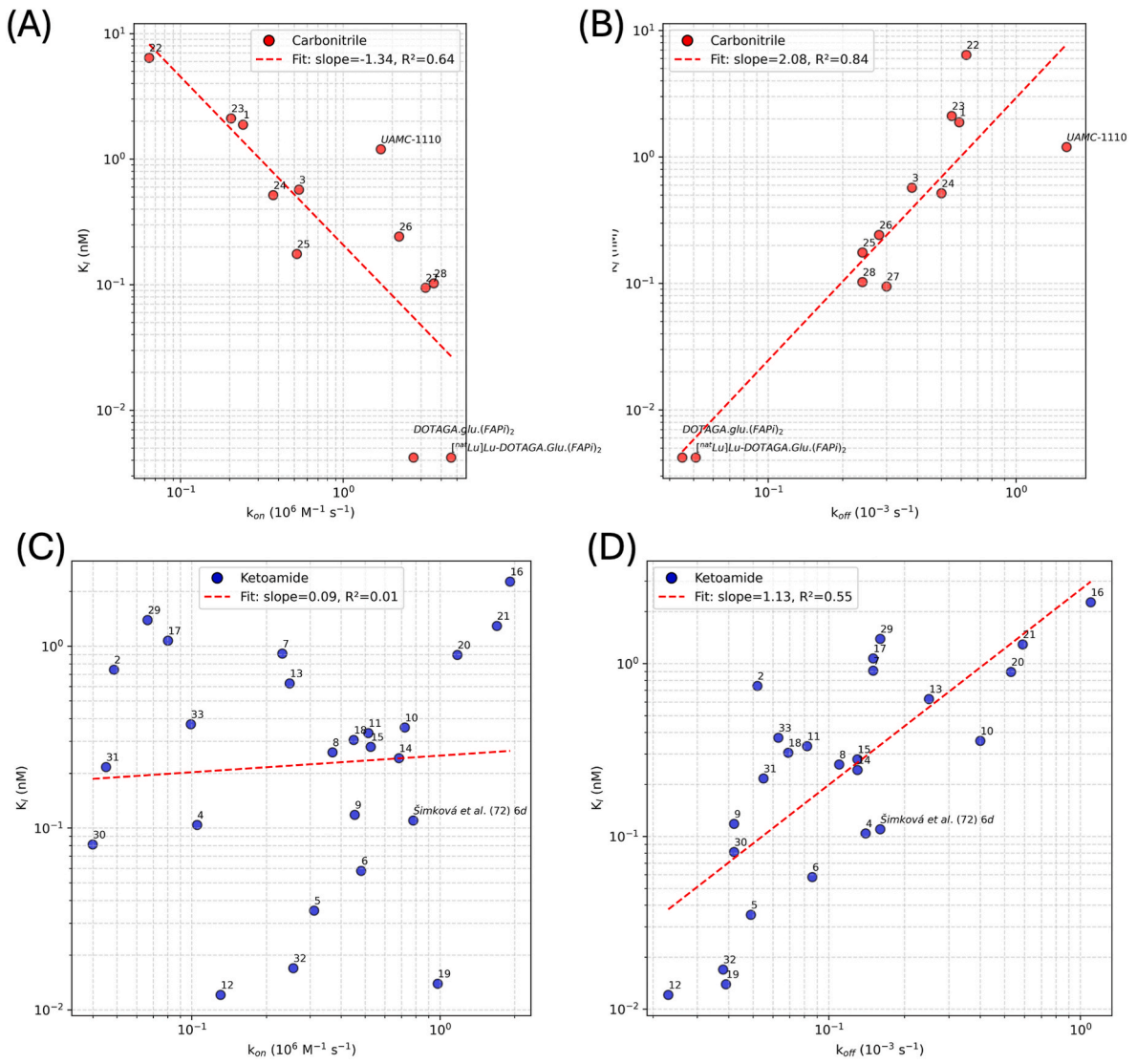

Fig. 2. Warhead-dependent relationships between affinity and binding kinetics. (A–D) Log-log plots of inhibitor affinity (K_i, nM) versus association rate (k_{on}, 10^6 M^{-1} s^{-1}) and dissociation rate (k_{off}, 10^{-3} s^{-1}) for FAPIs grouped by warhead: carbonitriles (red, A–B) and α-ketoamides (blue, C–D). Each point is the mean of n = 3 independent replicates; selected compounds are annotated. Dashed lines show robust linear regression fits with the corresponding R^2 and slope indicated in the legends.

trend (slope, $\log_{10}$-$\log_{10}$ = 0.35; 95 % CI -0.05 – 0.75; R^2 = 0.08; Fig. 3), suggesting that compounds with faster association rates also tend to dissociate more rapidly, albeit with substantial scatter. Monomeric carbonitrile FAPIs cluster in the upper region, reflecting their generally high k_{off}, but span a wide range of k_{on} values. For example, **1**, **22**, **23**, and **24** show only marginally reduced k_{off} relative to **UAMC-1110** yet have disproportionately lower k_{on}, resulting in poorer overall affinity and suggesting an unstable enzyme-inhibitor intermediate. In contrast, **25**–**28** combine slower dissociation with maintained or improved association rates, producing longer residence times and tighter binding, although none match the exceptionally low k_{off} of the dimeric **DOTAGA.Glu.(FAPi)$_2$** reference.

Most α-ketoamide analogues fall into the lower-left quadrant, characterized by both slow on- and off-rates. Exceptions include **10** and **16** (tetrahydrofuranyl warheads) and **20** and **21** (quinoline-8 substitution), which deviate toward higher k_{on} and k_{off}. Among monomeric α-ketoamides, **19** stands out: it combines a k_{off} similar to the dimeric FAPI reference (**DOTAGA.Glu.(FAPi)$_2$**) with one of the highest k_{on} values in its class.

As an orthogonal validation, we compared K_i values obtained from the Morrison equation applied to steady-state progress-curve velocities with those calculated from k_{off}/k_{on}. For the majority of compounds, the two approaches agreed closely (Table 7), underscoring the reliability of both our JDA and progress-curve assays. However, a subset of very high-affinity FAPIs (**4**–**6**, **32**) showed 5–10x lower K_i by Morrison analysis than by k_{off}/k_{on}.

3.6. *Computational docking corroborates experimental kinetic profiles of FAPIs*

Before examining FAPI docking, we first investigated how α-ketoamide warheads interact with the oxyanion hole. In the SARS-CoV-2 Mpro co-crystal (PDB: 6Y2G), the α-ketoamide's hydroxyl forms hydrogen bonds with the catalytic histidine and a nearby water molecule (Fig. 4) [102]. Mechanistically, histidine first deprotonates the catalytic cysteine, that attacks the α-keto carbonyl to form a tetrahedral intermediate; in which the oxyanion is stabilized by ionic interaction with the positively charged histidine. Lastly, the histidine protonates the oxyanion, yielding the covalent enzyme-inhibitor complex [103]. Because no leaving group departs, this intermediate closely resembles

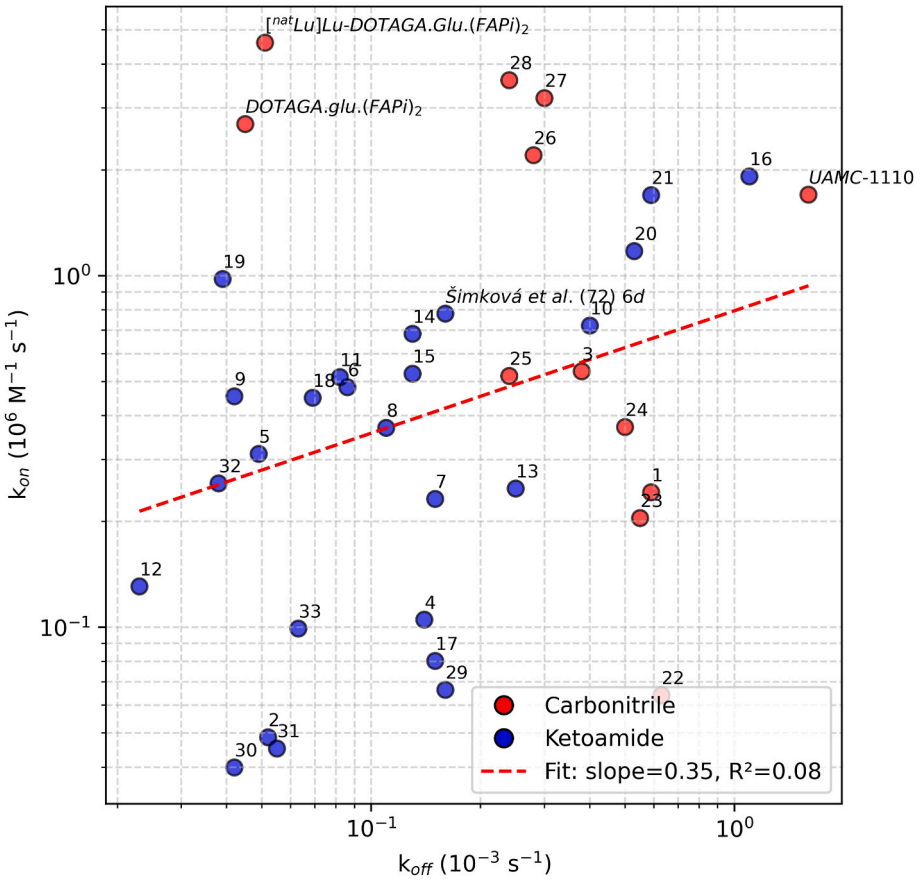

Fig. 3. Correlation of association (k_{on}) and dissociation (k_{off}) rate constants for FAPIs. Scatter plot of k_{off} (10^{-3} s^{-1}) versus k_{on} (10^{6} M^{-1} s^{-1}) on log scales for 35 in-house developed FAPIs (red circles: carbonitrile warheads; blue circles: α-ketoamide warheads) and four reference compounds. Each point is labeled by its identifier. The dashed red line represents a linear regression fit with the corresponding R^2 and slope indicated in the legend.

the final covalent adduct, unlike peptide substrates, whose amine leaving group must accept a proton from histidine. This mechanistic distinction is consistent with the catalytic process of serine proteases as summarized by Hedstrom et al. [104].

Docking (Fig. 5A) reveals two interactions as seen in the α-ketoamide crystal structure: the oxyanion is stabilized through an ionic interaction with H734 and can engage in a hydrogen bond with a water molecule, due to its solvent accessibility. Interestingly, warhead selection shifts the oxyanion-hole location. **UAMC-1110**, featuring a nitrile warhead, aligns with DPP4-inhibitors such as the **decapeptide** (PDB: 1R9N) and **vildagliptin** (PDB: 3W2T), positioning its nitrile to accept hydrogen bonds from the Y541 hydroxyl and the Y625 backbone [100,105]. In α-ketoamide FAPIs, the amide oxygen occupies the same pocket, preserving both hydrogen bonds and the engagement of the oxyanion-hole as observed in the SARS-CoV-2 Mpro structure.

All docked α-ketoamide FAPIs adopt a conserved binding mode in which the pyrrolidine ring nestles into a hydrophobic pocket lined by aromatic residues, similar to the binding pose of **vildagliptin** in DPP4. Incorporation of fluorine atoms on the pyrrolidine introduces possible halogen bonds or halogen–π interactions with Y625, Y656 and Y660, interactions that have been observed in related proteases, and may even contribute to selectivity [106,107].

Beyond the pyrrolidine, each warhead's aromatic substituent engages the S2′-S3′ region through π-π stacking with Y541, W621 or W623. Different stabilizing interactions are observed. The dimethoxybenzene group can form hydrogen bonds with N539 and Y745, whereas the benzotriazolyl ring orients to interact with V540, W623, and G626. Introducing a methyl group to generate the D-alanine derivative potentially enables hydrophobic contacts with F350 or Y660. The oxygen atom of the pyrrolidine amide is oriented toward the protein surface, as in the binding pose of **vildagliptin**, and might form a hydrogen bond with R123.

Additionally, a hydrogen is predicted between the quinoline nitrogen and Y124. The propoxy spacer between quinoline and piperazine exhibits conformational flexibility, resulting in diverse binding conformations of this region (Fig. 5B). In all piperazine derivatives, tertiary or quaternary, the positively charged nitrogen is oriented toward the solvent. Across all α-ketoamide-based compounds, the sp^2-hybrydized oxygen attached to the piperazine ring forms hydrogen bonds with F350 and F351. Finally, the Boc group and iodobenzene moiety could undergo hydrophobic interactions with L375 and F579, while the iodobenzene substituent could also participate in halogen bonding with E396 and A397.

4. Discussion

In this work we established a novel, robust *in vitro* workflow for measuring the dissociation rate constant (k_{off}) of FAPIs. The IC_{50}, while historically prevalent, fails to accurately reflect ligand affinity in tight-binding scenarios and does not capture the binding dynamics that govern target engagement *in vivo*. Given the high-affinity nature of FAPIs, IC_{50} values become increasingly misleading, necessitating alternative approaches. While surface-plasmon resonance (SPR) and grating-coupled interferometry (GCI) are well-established assays to determine these constants [108,109], slow, tight-binding conditions demand extensive optimization (ligand density, mass transport, rebinding, baseline drift) to obtain reliable rates [110]. Instead, the platform suggested here couples jump-dilution assays (JDAs) as the primary readout

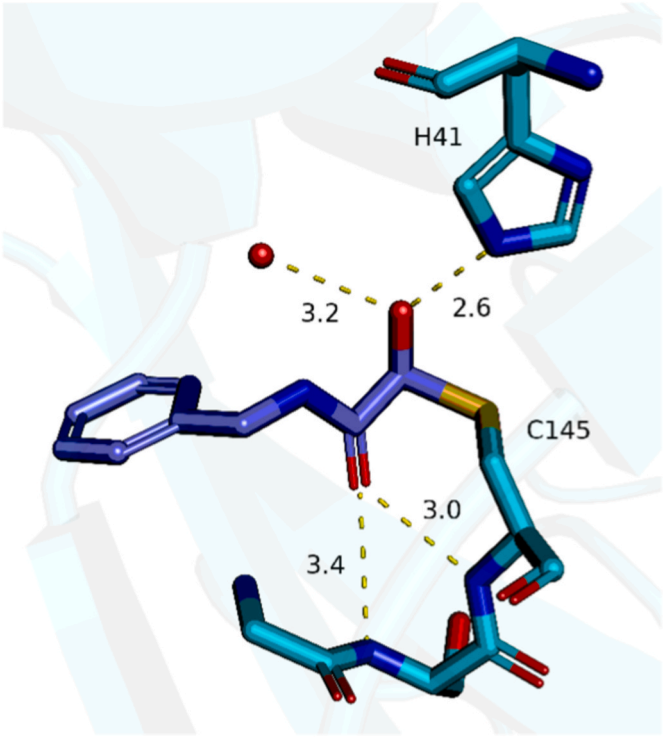

Fig. 4. Crystal structure (PDB: 6Y2G) of SARS-CoV-2 Mpro covalently bound to α-ketoamide inhibitor via C145. For clarity, only a portion of the ligand is shown in purple. Two hydrogen bond interactions involving the hydroxyl group with H41 and a water molecule are depicted, along with two additional hydrogen bonds formed by the amide oxygen. Hydrogen atoms are omitted, as their positions cannot be resolved in X-ray crystal structures. The distances are shown in angstrom.

for k_{off}, complemented with progress curve assays for k_{on}. JDAs are commonly used to evaluate the reversibility of inhibitors [72], but they are also suited for the determination of k_{off}. In this work, we tailored standard JDA practice for slow tight-binding conditions.

A cornerstone of this workflow was access to ultrapure, stable and highly active recombinant human (rhFAP). After optimizing expression and purification, the Freestyle™ 293-F-derived rhFAP production reported here achieved ≥99 % purity and excellent specific activity, exceeding prior reports using insect-cell systems [4,15,31]. The minor difference in K_m and k_{cat} for substrate B relative to prior work can be attributed to (i) the different substrate batch, and (ii) production of rhFAP from mammalian cells instead of insect cells [87]. The high-quality rhFAP allowed the use of picomolar enzyme concentrations in the JDA. Together with the use of a higher-affinity substrate (De Decker et al. substrate 6c [87]) compared with the commercial ZGP-AMC, this enables lower final inhibitor concentrations compared with what is generally used, typically at or below the predicted $K_{i,app}$ [111,112]. In practice, no single inhibitor concentration [I] fits all tight-binding inhibitors: we empirically balanced higher [I] to increase preincubation occupancy against lower [I] to preserve signal window after dilution and ensure visible curvature. This trade-off is intrinsic to JDAs and should be tuned per inhibitor-enzyme pair [73]. This step was essential to obtain trustworthy JDA curves, ensuring the achievement of proper curvature during the JDA, a requirement for accurate determination of k_{off} [73]. The head-to-head comparison of two literature reference FAPIs with GCI and SPR confirmed that the JDA reliably estimates k_{off}.

Among clinically evaluated carbonitrile tracers, the peptide-based reference **FAP-2286** ($\pm^{nat}$Lu) dissociated too rapidly to allow reliable k_{off} measurement by JDA. This highlights how incorporation of electrophilic warheads (in this study: carbonitrile or α-ketoamide) substantially prolongs target engagement compared with a simple peptide backbone. Accordingly, while the promising preclinical and clinical results of **FAP-2286** suggest that factors beyond target residence time contribute significantly to antitumor efficacy, warhead-containing FAPIs may still represent a superior theranostic approach. Their prolonged target engagement could facilitate the development of matched diagnostic-therapeutic pairs with sustained tumor retention [55,101,113,114].

FAPI-74 exhibited a slightly lower dissociation rate compared with **UAMC-1110** [78], despite bearing a bulky chelator on the quinoline C6 side chain, indicating a stabilizing impact of certain payloads at this position. In contrast, the dimeric compound **DOTAGA.Glu.(FAPi)$_2$** ($\pm^{nat}$Lu) was the only carbonitrile FAPI in our panel to reach a considerably long residence time (τ), comparable to some α-ketoamide FAPIs [34,35]. This is consistent with reports on **Bi-/TriOncoFAP** where multivalency improves apparent potency and cellular uptake in engineered FAP-overexpressing models [115,116]. Mechanistically, such gains might arise from avidity effects, i.e. reduced effective k_{off} and/or enhanced local rebinding, but the relative contributions remain to be clarified for FAP. Regarding **FAPI-mFS**, which combines a carbonitrile warhead with an aryl fluorosulfate (SuFEx) electrophile, Cui et al. demonstrated covalent engagement of FAP, rather than true irreversibility per se [117]. In line with that distinction, the JDA shows clear time-dependent recovery of FAP activity over several hours, yielding a finite k_{off} using this method that is significantly higher than the rate reported by SPR [117]. Overall, it seems that linking two FAPI units (each with its own warhead) to harness avidity appears more effective for achieving durable target engagement than stacking multiple

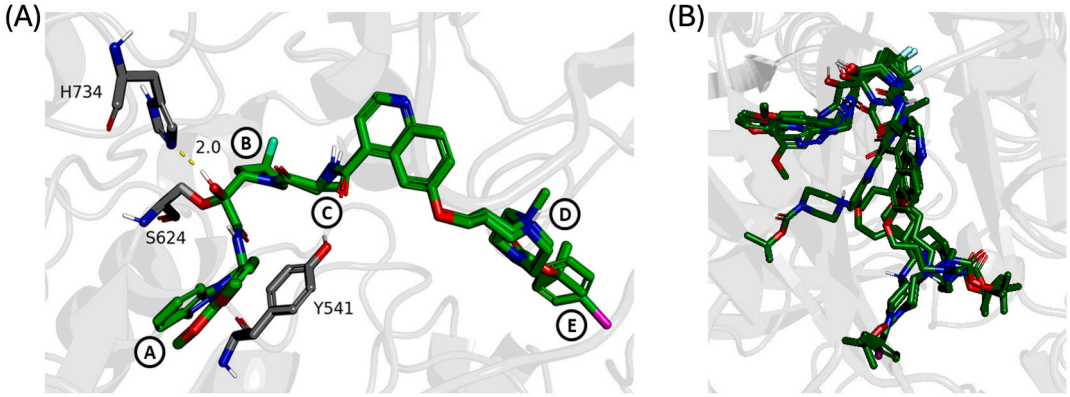

Fig. 5. (**A**) Overlay of docked poses for seven α-ketoamide-based FAPIs in the FAP active site, highlighting five structural variations: A) dimethoxybenzene or benzotriazolyl; B) fluorine or hydrogen atoms; C) glycine or D-alanine; D) piperazine or methyl-piperazine; E) Boc-protecting group or iodobenzene. The distances are shown in angstrom. (**B**) The binding poses of the covalently docked compounds before post-processing.

electrophiles on a single ligand.

The kinetic profiling of 35 in-house developed FAPIs revealed that warhead type is the principal determinant of residence time. Carbonitrile warheads generally dissociate rapidly, yielding a short τ, whereas α-ketoamide warheads dramatically prolong τ. Within the α-ketoamide series, benzotriazolyl and difluoromethoxyphenyl substituents on the warhead achieved the longest τ, up to 12 h (**12**), albeit with scaffold-dependent nuances between a quaternary ammonium vs a tertiary amine at quinoline C6. Conversely, tetrahydrofuranyl substituents (**10**, **16**) destabilize binding likely due to poor accommodation in the S2' pocket. The wide dynamic τ range underscores how subtle alterations in warhead electronics and sterics can tune binding lifetimes by over an order of magnitude. Ranking α-ketoamide substituents by electrophilicity (electron-withdrawing capacity) revealed no correlation with τ.

Substituent differences of the quinoline C6 likewise modulate τ. A small aliphatic cationic linker at C6 (**17**) has little to no impact on τ compared with the unsubstituted reference in α-ketoamide FAPIs. However, in carbonitrile FAPIs, whose baseline τ are generally shorter, the same linker (**1**, **22**) produces a measurable increase in τ. Since docking places both warhead classes in similar active-site orientations, the observed gains are likely not due to differences in warhead positioning but might be related to the spacer's conformational flexibility, enabling more effective engagement with peripheral pockets in compounds lacking strong intrinsic binding. Replacing that aliphatic linker with a more polar PEG_3 chain (**25**) further extends τ, possibly by engaging with polar peripheral S2/S3 subsites. Relocation of a substituent from quinoline C6 to C8 (**20**, **21**) impaired τ by a factor three, similar to what Lindner et al. found regarding the influence of quinoline C7 on affinity, highlighting that the C6 locus resides in a permissive cavity whereas C7 or C8 substitutions encounter steric or electrostatic penalties [29]. Extending the quinoline C6 short aliphatic substituent with a piperazine (**18**) further improves τ, which is consistent as well with Lindner et al.'s observation that heterocyclic side chains at this position boost tumor retention [29]. Our preliminary kinetic SAR data suggests that finetuning the substituent attached to the piperazine ring may further improve τ.

When looking at the pyrrolidine ring, difluorination of C2 consistently extends τ in dimethoxybenzylated α-ketoamide FAPIs (**5**, **17**, **29** vs **30**, **31**, **32**), in line with earlier reports where pyrrolidine fluorination improved FAP binding and tracer performance in both SAR and *in vivo* biodistribution studies [27,118,119]. Unexplainably, the reverse effect was observed on α-ketoamide FAPIs with a benzotriazolyl substituent (**12** vs **4**). Lastly, we proved that switching the Gly-Pro motif (**32**) for a D-Ala-Pro motif (**33**) negatively affects τ, as has been demonstrated in literature regarding affinity as well [120,121]. Mechanistically, FAP's S1 subsite houses a hydrophobic pocket lined by Tyr625, Val650, and Trp653 that selectively accommodates P1 proline, whereas S2 tolerates small D-amino acids or glycine. While substituting Gly with D-Ala markedly enhances selectivity for FAP over PREP, this modification may introduce steric or electrostatic penalties. It remains to be determined whether, *in vivo*, this benefit outweighs the drawback of a reduced τ [120–122]. The introduction of a DOTA-based chelator had a measurable impact on target residence time, as described in Brzeminski et al. [77], whereas loading the chelator with ^{nat}Lu (**34** vs **35**) did not further alter the kinetic behavior.

Overall, JDAs provide a rapid, cost-effective means to estimate k_{off} and, by extension, offer a qualitative readout of *in vivo* target residence time [57,59,61,65]. Limitations remain though, as some of the error bars remain considerable, especially for FAPIs with low k_{off}, resulting in wider error bars that can mask subtle improvements in τ. Much of this variability stems from the manual handling of sub-microliter volumes and timing fluctuations inherent to the JDA. Adopting automated liquid-handling systems and integrated plate-reader workflows would minimize pipetting variability, standardize incubation times, and greatly increase both precision and throughput [62]. A further complexity is that FAP inhibitors with α-ketoamide warheads can also occur in a cyclic form that is in tautomeric equilibrium with the parent structure. Likewise, in aqueous media, the electrophilic ketone group can be in equilibrium with its hydrated congener. Both factors thus complicate the accurate determination of free FAPI concentration and potentially introduce additional variability [75]. Future research could focus on even further reducing the enzyme concentration and optimizing assay settings to support stable signals in prolonged runs (>10 h).

The progress curve assays, which follow the time-dependent approach to inhibited steady state, allowed to estimate k_{on} and K_i for each FAPI in a single experiment. These measurements complement the JDAs. Across both warhead scaffolds, k_{on} varied widely, spanning nearly two orders of magnitude. All carbonitrile FAPIs were well described by the one-step inhibition model, consistent with the clear inverse correlation between k_{on} and K_i. In contrast, several α-ketoamide FAPIs follow a different, two-step inhibition model, which might explain why the correlation between k_{on} and K_i essentially disappeared for these FAPIs, as the rate-limiting step in the forward reaction probably is k_{for}. Conversely to carbonitrile FAPIs, where both k_{on} and k_{off} predict overall affinity, the K_i in α-ketoamide FAPIs seems to mainly depend on k_{off}. Hence, k_{off} is not only a useful metric to determine τ, but also a good predictor of overall affinity, especially in the case of α-ketoamide FAPIs. A subset of α-ketoamide FAPIs produced concave-up k_{obs} versus [I] plots, inconsistent with the simple one- or two-step models, indicative of tight-binding experimental conditions according to Kuzmic et al. [123].

When looking at the k_{off}/k_{on} plot of all FAPIs together, a modest positive slope emerges, pointing to the kinetic "speed-stability" trade-off observed in many enzyme-inhibitor systems. The dimeric carbonitrile reference **[^{nat}Lu] Lu-DOTAGA.Glu.(FAPi)$_2$** defies this trend by pairing one of the highest measured k_{on} rates ($4.6 \times 10^6\ M^{-1}\ s^{-1}$) with a low k_{off} ($0.051 \times 10^{-3}\ s^{-1}$), creating an almost ideal kinetic profile for rapid target engagement and prolonged residence time. This performance stems from avidity rather than simultaneous dual-site binding, which is sterically unfeasible based on current insights. Rapid rebinding of the second moiety effectively lowers the observed k_{off}. Monomeric α-ketoamide **19** approaches this profile, combining a comparably low k_{off} with a higher k_{on} than its α-ketoamide peers, making it a promising scaffold to explore multimerization with, aimed at further reducing k_{off} without compromising k_{on}.

Importantly, even the fastest rates observed in this study fall well below the theoretical diffusion-limited maximum for k_{on} in an aqueous solution (10^8-$10^9\ M^{-1}\ s^{-1}$), implying that limiting factors such as desolvation, possible conformational rearrangement, and precise active-site alignment govern the true association rate. One practical consideration in our progress curve assays was gradual signal loss over extended (>6 h) measurements. Because substrate concentrations remained non-limiting, this decline might reflect partial rhFAP instability at 37 °C after several hours, surface adsorption or photobleaching of the substrate.

Having determined k_{on} and k_{off} for each FAPI, we compared the calculated K_i ($=k_{off}/k_{on}$) with the K_i obtained by fitting steady-state velocities from the progress curve assay to the Morrison equation. For FAPIs conforming to the one-step model, the two K_i values agreed closely, validating both the progress curve assay and JDA. For FAPIs following the two-step model (**10**, **16**–**18**, **21**), a systematic offset was observed. This reflects the assumptions made for the k_{off} and k_{on}, which do not accurately capture the conversion to the tighter complex EI*, while the Morrison equation accounts for the total equilibrium, one- or two-step model. The FAPIs exhibiting an atypical, concave-up k_{obs} vs [I] plot displayed a 5-10-fold difference between Morrison-derived K_i and the K_i predicted by k_{off}/k_{on}, typical of unmet pseudo-first order conditions. In addition, many of the progress curves for the higher-affinity FAPIs lacked datapoints with sufficiently low [I] because it would require even longer assay durations and improved enzyme stability, substantially challenging Morrison model fitting. This led to uncertainty about the K_i value obtained from the Morrison model for these specific FAPIs.

The covalent docking results provide novel insights into the binding poses of FAPIs containing the α-ketoamide warhead. The docking results let us hypothesize that for the α-ketoamide warhead the oxyanion (formed by the attack of the catalytic serine) binds to a different pocket than the oxyanion formed on the scissile bond during peptide turnover. This is consistent with previous experimental and computational studies [102,103]. The conserved binding orientations of the docked FAPIs correlate with their relatively low k_{off} rates. These findings could be further validated through experimental studies and/or molecular dynamics simulations of the covalently bound complexes.

In summary, we have established and validated a JDA to measure k_{off} that is low-cost, reproducible and amenable to high-throughput use. Deployed at scale, this readout enables screening across diverse FAPI chemotypes, ultimately increasing the likelihood of successful therapeutic breakthroughs in the FAPI field. We anticipate that widespread adoption of this method will replace reliance on IC_{50} for early-stage discovery, particularly as IC_{50} collapses under tight-binding conditions and fails to discriminate between highly potent candidates. Instead, prioritizing k_{off} – and thus residence time – will more accurately predict *in vivo* tumor retention. A complementary progress curve assay yields k_{on}, and permits estimation of K_i, enabling full-circle kinetic SAR rather than pure static affinity ranking. Beyond FAP, this kinetic toolkit offers a generalizable approach for protease-targeted drug discovery: the used assays provide a rapid, cost-effective means to conduct kinetic SAR that (i) estimates *in vivo* target dynamics and (ii) moves beyond static affinity metrics [62]. Medicinal chemists can strategically pursue modifications that modulate k_{on} or k_{off} independently. Lastly, while the docking studies provide useful mechanistic hypotheses, co-crystal structures of FAP with high-affinity α-ketoamide FAPIs will be crucial to confirm predicted binding modes and water-mediated interactions.

5. Conclusion

In summary, we have created and validated a high-throughput kinetic screening platform that integrates jump-dilution assays and progress curve analyses to directly and reliably measure k_{off}, k_{on}, and derive K_i at subnanomolar enzyme concentrations. Benchmarked against GCI and SPR, this workflow overcomes the variability and artefacts inherent to IC_{50} assays when working with slow, tight-binding inhibitors, delivering rate constants that better estimate residence time and true binding affinity. Its straightforward, automation-compatible format and minimal material requirements make it ideally suited for large-scale kinetic SAR studies of FAPIs – and protease inhibitors in general – early in the discovery process. By shifting the focus from static potency snapshots to dynamic kinetic parameters, this approach will sharpen early-stage decision-making and enhance the prediction of *in vivo* target residence time.

CRediT authorship contribution statement

Emile Verhulst: Writing – review & editing, Writing – original draft, Visualization, Validation, Software, Project administration, Methodology, Investigation, Formal analysis, Data curation, Conceptualization. **Pawel Brzeminski:** Writing – review & editing, Visualization, Investigation. **Anke de Groot:** Writing – review & editing, Visualization, Investigation, Formal analysis. **Joep W. Wals:** Writing – review & editing, Visualization, Investigation, Formal analysis, Data curation. **Robbe Michiels:** Visualization, Investigation, Formal analysis, Data curation. **Adrian Fabisiak:** Writing – review & editing, Investigation. **Jari Thys:** Writing – review & editing, Investigation, Data curation. **Sergei Grintsevich:** Investigation. **Yentl Van Rymenant:** Investigation, Conceptualization. **Sarah Peeters:** Writing – review & editing, Methodology, Investigation. **Stijn Lambregts:** Investigation. **Yani Sim:** Project administration, Investigation. **Ruben Verstraete:** Writing – review & editing, Investigation, Formal analysis, Data curation. **Pieter Van Wielendaele:** Writing – review & editing, Validation, Formal analysis. **Maya Berg:** Writing – review & editing, Funding acquisition. **Filipe Elvas:** Writing – review & editing, Resources, Funding acquisition, Conceptualization. **Xaveer Van Ostade:** Writing – review & editing, Resources. **Frank Rösch:** Writing – review & editing, Resources. **Anne-Marie Lambeir:** Writing – review & editing, Visualization, Validation, Supervision, Methodology, Investigation, Formal analysis, Data curation, Conceptualization. **Hans De Winter:** Supervision, Resources, Funding acquisition, Formal analysis. **Pieter Van Der Veken:** Writing – review & editing, Resources, Methodology, Investigation, Funding acquisition, Formal analysis, Conceptualization. **Ingrid De Meester:** Writing – review & editing, Writing – original draft, Supervision, Resources, Project administration, Methodology, Funding acquisition, Formal analysis, Conceptualization.

Declaration of competing interest

The authors declare that they have no known competing financial interests or personal relationships that could have appeared to influence the work reported in this paper.

Acknowledgements

The authors thank Jakob Raymaekers (Assistant Prof. of Applied Mathematics, University of Antwerp) for valuable advice on the data processing of the jump-dilution assays and Fernanda dos Reis Rocho (Medical Biochemistry, University of Antwerp) for valuable discussions. This work was co-financed by grant FWO-SB S003525N, grant FWO-MZW, grant 11P4L24N and grant 11PCL24N from the Research Foundation – Flanders; grant 101073231 from the Marie Skłodowska-Curie Action (OncoProTools); grant MSCA-2023-PF-01-101155227 and grant MSCA-2023-PF-01-101155555 from the Marie Skłodowska-Curie Action; grant 542300002 and tenure track grant FFB210263 from the University Research Fund (BOF).

Appendix A. Supplementary data

Supplementary data to this article can be found online at https://doi.org/10.1016/j.ejmech.2025.118494.

Data availability

Data will be made available on request.

References

[1] P. Garin-Chesa, L.J. Old, W.J. Rettig, Cell surface glycoprotein of reactive stromal fibroblasts as a potential antibody target in human epithelial cancers, Proc. Natl. Acad. Sci. U. S. A 87 (18) (1990) 7235–7239, https://doi.org/10.1073/pnas.87.18.7235.

[2] T. Kelly, S. Kechelava, T.L. Rozypal, K.W. West, S. Korourian, Seprase, a membrane-bound protease, is overexpressed by invasive ductal carcinoma cells of human breast cancers, Mod. Pathol. 11 (9) (1998) 855–863. From NLM.

[3] M.L. Piñeiro-Sánchez, L.A. Goldstein, J. Dodt, L. Howard, Y. Yeh, H. Tran, W. S. Argraves, W.T. Chen, Identification of the 170-kDa melanoma membrane-bound gelatinase (seprase) as a serine integral membrane protease, J. Biol. Chem. 272 (12) (1997) 7595–7601, https://doi.org/10.1074/jbc.272.12.7595. From NLM.

[4] S. Sun, C.F. Albright, B.H. Fish, H.J. George, B.H. Selling, G.F. Hollis, R. Wynn, Expression, purification, and kinetic characterization of full-length human fibroblast activation protein, Protein Expr. Purif. 24 (2) (2002) 274–281, https://doi.org/10.1006/prep.2001.1572.

[5] W.J. Rettig, P.G. Chesa, H.R. Beresford, H.J. Feickert, M.T. Jennings, J. Cohen, H. F. Oettgen, L.J. Old, Differential expression of cell surface antigens and glial fibrillary acidic protein in human astrocytoma subsets, Cancer Res. 46 (12 Pt 1) (1986) 6406–6412. From NLM.

[6] A.A. Fitzgerald, L.M. Weiner, The role of fibroblast activation protein in health and malignancy, Cancer Metastasis Rev. 39 (3) (2020) 783–803, https://doi.org/10.1007/s10555-020-09909-3. From NLM.

[7] M. Levy, G. McCaughan, G. Marinos, M. Gorrell, Intrahepatic expression of the hepatic stellate cell marker fibroblast activation protein correlates with the degree of fibrosis in hepatitis C virus infection, Liver 22 (2) (2002) 93–101, https://doi.org/10.1034/j.1600-0676.2002.01503.x.

[8] A.-T. Yang, Y.-O. Kim, X.-Z. Yan, H. Abe, M. Aslam, K.-S. Park, X.-Y. Zhao, J.-D. Jia, T. Klein, H. You, et al., Fibroblast activation protein activates macrophages and promotes parenchymal liver inflammation and fibrosis, CMGH 15 (4) (2023) 841–867, https://doi.org/10.1016/j.jcmgh.2022.12.005. (Accessed 20 March 2025).

[9] B.-J. Ke, S. Abdurahiman, F. Biscu, G. Zanella, G. Dragoni, S. Santhosh, V. De Simone, A. Zouzaf, L. van Baarle, M. Stakenborg, et al., Intercellular interaction between FAP+ fibroblasts and CD150+ inflammatory monocytes mediates fibrostenosis in Crohn's disease, J. Clin. Immunoassay 134 (16) (2024), https://doi.org/10.1172/JCI173835.

[10] W.J. Rettig, P. Garin-Chesa, J.H. Healey, S.L. Su, H.L. Ozer, M. Schwab, A. P. Albino, L.J. Old, Regulation and heteromeric structure of the fibroblast activation protein in normal and transformed cells of mesenchymal and neuroectodermal origin, Cancer Res. 53 (14) (1993) 3327–3335. Article. Scopus.

[11] E. Puré, R. Blomberg, Pro-tumorigenic roles of fibroblast activation protein in cancer: back to the basics, Oncogene 37 (32) (2018) 4343–4357, https://doi.org/10.1038/s41388-018-0275-3. From NLM.

[12] M.J. Scanlan, B.K. Raj, B. Calvo, P. Garin-Chesa, M.P. Sanz-Moncasi, J.H. Healey, L.J. Old, W.J. Rettig, Molecular cloning of fibroblast activation protein alpha, a member of the serine protease family selectively expressed in stromal fibroblasts of epithelial cancers, Proc. Natl. Acad. Sci. U. S. A 91 (12) (1994) 5657–5661, https://doi.org/10.1073/pnas.91.12.5657. From NLM.

[13] L.A. Goldstein, G. Ghersi, M.L. Piñeiro-Sánchez, S. Monica, Y. Yeh, D. Flessate, W.-T. Chen, Molecular cloning of seprase: a serine integral membrane protease from human melanoma, BBA - Mol. Basis of Disease 1361 (1) (1997) 11–19, https://doi.org/10.1016/S0925-4439(97)00032-X.

[14] K.N. Lee, K.W. Jackson, V.J. Christiansen, K.H. Chung, P.A. McKee, A novel plasma proteinase potentiates α2-antiplasmin inhibition of fibrin digestion, Blood 103 (10) (2004) 3783–3788, https://doi.org/10.1182/blood-2003-12-4240.

[15] K.N. Lee, K.W. Jackson, V.J. Christiansen, C.S. Lee, J.G. Chun, P.A. McKee, Antiplasmin-cleaving enzyme is a soluble form of fibroblast activation protein, Blood 107 (4) (2006) 1397–1404, https://doi.org/10.1182/blood-2005-08-3452. From NLM.

[16] A. Šimková, P. Bušek, A. Šedo, J. Konvalinka, Molecular recognition of fibroblast activation protein for diagnostic and therapeutic applications, BBA - Proteins Proteom 1868 (7) (2020), https://doi.org/10.1016/j.bbapap.2020.140409.

[17] P.J. Collins, G. McMahon, P. O'Brien, B. O'Connor, Purification, identification and characterisation of seprase from bovine serum, Int. J. Biochem. Cell Biol. 36 (11) (2004) 2320–2333, https://doi.org/10.1016/j.biocel.2004.05.006.

[18] M. Javidroozi, S. Zucker, W.-T. Chen, Plasma seprase and DPP4 levels as markers of disease and prognosis in cancer, Dis. Markers 32 (2012) 706–745, https://doi.org/10.3233/DMA-2011-0889.

[19] F.M. Keane, T.-W. Yao, S. Seelk, M.G. Gall, S. Chowdhury, S.E. Poplawski, J. H. Lai, Y. Li, W. Wu, P. Farrell, et al., Quantitation of fibroblast activation protein (FAP)-specific protease activity in mouse, baboon and human fluids and organs, FEBS Open Bio. 4 (1) (2014) 43–54, https://doi.org/10.1016/j.fob.2013.12.001.

[20] E. Verhulst, D. Garnier, I. De Meester, B. Bauvois, Validating cell surface proteases as drug targets for cancer therapy: what do we know, and where do we go? Cancers (Basel) 14 (3) (2022).

[21] K. Narra, S.R. Mullins, H.-O. Lee, B. Strzemkowski-Brun, K. Magalong, V. J. Christiansen, P.A. McKee, B. Egleston, S.J. Cohen, L.M. Weiner, et al., Phase II trial of single agent Val-boroPro (talabostat) inhibiting fibroblast activation protein in patients with metastatic colorectal cancer, Cancer Biol. Ther. 6 (11) (2007) 1691–1699, https://doi.org/10.4161/cbt.6.11.4874.

[22] R.D. Hofheinz, S.E. Al-Batran, F. Hartmann, G. Hartung, D. Jäger, C. Renner, P. Tanswell, U. Kunz, A. Amelsberg, H. Kuthan, et al., Stromal antigen targeting by a humanised monoclonal antibody: an early phase II trial of sibrotuzumab in patients with metastatic colorectal cancer, in: Onkologie, Onkologie, vol. 26, 2003, pp. 44–48.

[23] A.M. Scott, G. Wiseman, S. Welt, A. Adjei, F.T. Lee, W. Hopkins, C.R. Divgi, L. H. Hanson, P. Mitchell, D.N. Gansen, et al., A Phase I dose-escalation study of sibrotuzumab in patients with advanced or metastatic fibroblast activation protein-positive cancer, Clin. Cancer Res. 9 (5) (2003) 1639–1647. From NLM.

[24] J. Nemunaitis, S.J. Vukelja, D. Richards, C. Cunningham, N. Senzer, J. Nugent, H. Duncan, B. Jones, E. Haltom, M.J. Uprichard, Phase I trial of PT-100 (PT-100), A cytokine-inducing small molecule, following chemotherapy for solid tumor malignancy, Cancer Invest. 24 (6) (2006) 553–561, https://doi.org/10.1080/07357900600894732.

[25] O. Ryabtsova, K. Jansen, S. Van Goethem, J. Joossens, J.D. Cheng, A.-M. Lambeir, I. De Meester, K. Augustyns, P. Van der Veken, Acylated Gly-(2-cyano) pyrrolidines as inhibitors of fibroblast activation protein (FAP) and the issue of FAP/prolyl oligopeptidase (PREP)-selectivity, Bioorg. Med. Chem. Lett 22 (10) (2012) 3412–3417, https://doi.org/10.1016/j.bmcl.2012.03.107.

[26] K. Jansen, L. Heirbaut, J.D. Cheng, J. Joossens, O. Ryabtsova, P. Cos, L. Maes, A.-M. Lambeir, I. De Meester, K. Augustyns, et al., Selective inhibitors of Fibroblast Activation Protein (FAP) with a (4-Quinolinoyl)-glycyl-2-cyanopyrrolidine scaffold, ACS Med. Chem. Lett. 4 (5) (2013) 491–496, https://doi.org/10.1021/ml300410d. PubMed.

[27] K. Jansen, L. Heirbaut, R. Verkerk, J.D. Cheng, J. Joossens, P. Cos, L. Maes, A.-M. Lambeir, I. De Meester, K. Augustyns, et al., Extended structure–activity relationship and pharmacokinetic investigation of (4-Quinolinoyl)glycyl-2-cyanopyrrolidine inhibitors of Fibroblast Activation Protein (FAP), J. Med. Chem. 57 (7) (2014) 3053–3074, https://doi.org/10.1021/jm500031w.

[28] A. Loktev, T. Lindner, W. Mier, J. Debus, A. Altmann, D. Jäger, F. Giesel, C. Kratochwil, P. Barthe, C. Roumestand, et al., A tumor-imaging method targeting cancer-associated fibroblasts, J. Nucl. Med. 59 (9) (2018) 1423–1429, https://doi.org/10.2967/jnumed.118.210435. PubMed.

[29] T. Lindner, A. Loktev, A. Altmann, F. Giesel, C. Kratochwil, J. Debus, D. Jäger, W. Mier, U. Haberkorn, Development of quinoline-based Theranostic ligands for the targeting of fibroblast activation protein, J. Nucl. Med. 59 (9) (2018) 1415–1422, https://doi.org/10.2967/jnumed.118.210443.

[30] F.L. Giesel, C. Kratochwil, T. Lindner, M.M. Marschalek, A. Loktev, W. Lehnert, J. Debus, D. Jäger, P. Flechsig, A. Altmann, et al., (68)Ga-FAPI PET/CT: biodistribution and preliminary dosimetry estimate of 2 DOTA-containing FAP-targeting agents in patients with various cancers, J. Nucl. Med. 60 (3) (2019) 386–392, https://doi.org/10.2967/jnumed.118.215913. PubMed.

[31] E.S. Moon, F. Elvas, G. Vliegen, S. De Lombaerde, C. Vangestel, S. De Bruycker, A. Bracke, E. Eppard, L. Greifenstein, B. Klasen, et al., Targeting fibroblast activation protein (FAP): next generation PET radiotracers using squaramide coupled bifunctional DOTA and DATA(5m) chelators, EJNMMI Radiopharm. Chem. 5 (1) (2020), https://doi.org/10.1186/s41181-020-00102-z. PubMed.

[32] E.S. Moon, S. Ballal, M.P. Yadav, C. Bal, Y. Van Rymenant, S. Stephan, A. Bracke, P. Van der Veken, I. De Meester, F. Roesch, Fibroblast activation Protein (FAP) targeting homodimeric FAP inhibitor radiotheranostics: a step to improve tumor uptake and retention time, Am. J. Nucl. Med. Mol. Imaging 11 (6) (2021) 476–491. From NLM.

[33] E.S. Moon, Y. Van Rymenant, S. Battan, J. De Loose, A. Bracke, P. Van der Veken, I. De Meester, F. Rösch, In vitro evaluation of the squaramide-conjugated fibroblast activation protein inhibitor-based agents AAZTA(5).SA.FAPi and DOTA.SA.FAPi, Molecules 26 (12) (2021) 3482, https://doi.org/10.3390/molecules26123482. PubMed.

[34] M. Martin, S. Ballal, M. Yadav, C. Bal, Y. Van Rymenant, J. De Loose, E. Verhulst, I. De Meester, P. Van Der Veken, F. Roesch, (Radio)synthesis and in vitro-evaluation of dimeric FAP-inhibitor based radiopharmaceuticals, J. Nucl. Med. 64 (supplement 1) (2023).

[35] M. Martin, S. Ballal, M.P. Yadav, C. Bal, Y. Van Rymenant, J. De Loose, E. Verhulst, I. De Meester, P. Van Der Veken, F. Roesch, Novel generation of FAP inhibitor-based homodimers for improved application in radiotheranostics, Cancers (Basel) 15 (6) (2023), https://doi.org/10.3390/cancers15061889. From NLM.

[36] L. Zhao, J. Chen, Y. Pang, K. Fu, Q. Shang, H. Wu, L. Sun, Q. Lin, H. Chen, Fibroblast activation protein-based theranostics in cancer research: a state-of-the-art review, Theranostics 12 (4) (2022) 1557–1569, https://doi.org/10.7150/thno.69475. PubMed.

[37] M. Tanc, N. Filippi, Y. Van Rymenant, S. Grintsevich, I. Pintelon, M. Verschuuren, J. De Loose, E. Verhulst, E.S. Moon, L. Cianni, et al., Druglike, 18F-labeled PET tracers targeting fibroblast activation protein, J. Med. Chem. 67 (9) (2024) 7068–7087, https://doi.org/10.1021/acs.jmedchem.3c02402.

[38] J. Millul, G. Bassi, J. Mock, A. Elsayed, C. Pellegrino, A. Zana, S.D. Plaza, L. Nadal, A. Gloger, E. Schmidt, et al., An ultra-high-affinity small organic ligand of fibroblast activation protein for tumor-targeting applications, Proc. Natl. Acad. Sci. U. S. A 118 (16) (2021), https://doi.org/10.1073/pnas.2101852118. Scopus.

[39] X. Qiu, Q. Gan, T. Ji, H. Xu, K. Cui, L. Yi, X. Yang, M.-F. Yang, Rational modifications on N-(4-quinolinoyl)-Gly-2-cyanopyrrolidine to develop fibroblast activation protein-targeted radioligands with improved affinity and tumor uptake, Eur. J. Med. Chem. 281 (2025), https://doi.org/10.1016/j.ejmech.2024.117011.

[40] A. Loktev, T. Lindner, E.M. Burger, A. Altmann, F. Giesel, C. Kratochwil, J. Debus, F. Marmé, D. Jäger, W. Mier, et al., Development of fibroblast activation protein-targeted radiotracers with improved tumor retention, J. Nucl. Med. 60 (10) (2019) 1421–1429, https://doi.org/10.2967/jnumed.118.224469. From NLM.

[41] A. Altmann, C. Kratochwil, F. Giesel, U. Haberkorn, Ligand engineering for theranostic applications, Curr. Opin. Chem. Biol. 63 (2021) 145–151, https://doi.org/10.1016/j.cbpa.2021.04.006. From NLM.

[42] D. Zboralski, F. Osterkamp, A.D. Simmons, A. Bredenbeck, A. Schumann, M. Paschke, N. Beindorff, A.M. Mohan, M. Nguyen, J. Xiao, et al., 571P preclinical evaluation of FAP-2286, a peptide-targeted radionuclide therapy (PTRT) to fibroblast activation protein alpha (FAP), Ann. Oncol. 31 (2020) S488, https://doi.org/10.1016/j.annonc.2020.08.685.

[43] Y. Pang, L. Zhao, J. Fang, J. Chen, L. Meng, L. Sun, H. Wu, Z. Guo, Q. Lin, H. Chen, Development of FAPI tetramers to improve tumor uptake and efficacy of FAPI radioligand therapy, J. Nucl. Med. 64 (9) (2023) 1449–1455, https://doi.org/10.2967/jnumed.123.265599. From NLM.

[44] X.-Y. Cui, Z. Li, Z. Kong, Y. Liu, H. Meng, Z. Wen, C. Wang, J. Chen, M. Xu, Y. Li, et al., Covalent targeted radioligands potentiate radionuclide therapy, Nature 630 (8015) (2024) 206–213, https://doi.org/10.1038/s41586-024-07461-6.

[45] H. Fu, J. Huang, T. Zhao, H. Wang, Y. Chen, W. Xu, Y. Pang, W. Guo, L. Sun, H. Wu, et al., Fibroblast activation protein-targeted radioligand therapy with 177Lu-EB-FAPI for metastatic radioiodine-refractory thyroid cancer: first-in-human, dose-escalation study, Clin. Cancer Res. 29 (23) (2023) 4740–4750, https://doi.org/10.1158/1078-0432.Ccr-23-1983. From NLM.

[46] L. Zhao, X. Wen, W. Xu, Y. Pang, L. Sun, X. Wu, P. Xu, J. Zhang, Z. Guo, Q. Lin, et al., Clinical evaluation of (68)Ga-FAPI-RGD for imaging of fibroblast activation protein and integrin α(v)β(3) in various cancer types, J. Nucl. Med. 64 (8) (2023) 1210–1217, https://doi.org/10.2967/jnumed.122.265383. From NLM.

[47] L. Greifenstein, A. Gunkel, A. Hoehne, F. Osterkamp, C. Smerling, C. Landvogt, C. Mueller, R.P. Baum, 3BP-3940, a highly potent FAP-targeting peptide for theranostics - production, validation and first in human experience with Ga-68 and Lu-177, iScience 26 (12) (2023), https://doi.org/10.1016/j.isci.2023.108541.

[48] J.M. Kelly, T.M. Jeitner, S. Ponnala, C. Williams, A. Nikolopoulou, S.G. DiMagno, J.W. Babich, A trifunctional Theranostic ligand targeting fibroblast activation Protein-α (FAPα), Mol. Imag. Biol. 23 (5) (2021) 686–696, https://doi.org/10.1007/s11307-021-01593-1.

[49] S. Puglioli, E. Schmidt, C. Pellegrino, L. Prati, S. Oehler, R. De Luca, A. Galbiati, C. Comacchio, L. Nadal, J. Scheuermann, et al., Selective tumor targeting enabled by picomolar fibroblast activation protein inhibitors isolated from a DNA-encoded affinity maturation library, Chem 9 (2) (2023) 411–429, https://doi.org/10.1016/j.chempr.2022.10.006.

[50] J. Millul, L. Koepke, G.R. Haridas, K.M.J. Sparrer, R. Mansi, M. Fani, Head-to-head comparison of different classes of FAP radioligands designed to increase tumor residence time: monomer, dimer, albumin binders, and small molecules vs peptides, Eur. J. Nucl. Med. Mol. Imag. 50 (10) (2023) 3050–3061, https://doi.org/10.1007/s00259-023-06272-7. From NLM Medline.

[51] H. Fu, J. Huang, L. Zhao, Y. Chen, W. Xu, J. Cai, L. Yu, Y. Pang, W. Guo, B. Su, et al., 177Lu-LNC1004 radioligand therapy in patients with end-stage metastatic cancers: a single-center, single-arm, phase II study, Clin. Cancer Res. 31 (8) (2025) 1415–1426, https://doi.org/10.1158/1078-0432.CCR-24-3918. From NLM Medline.

[52] J. Calais, FAP: the next billion dollar nuclear theranostics target? J. Nucl. Med. 61 (2) (2020) 163–165, https://doi.org/10.2967/jnumed.119.241232.

[53] R.P. Baum, E. Novruzov, T. Zhao, L. Greifenstein, V. Jakobsson, E. Perrone, A. Mishra, A. Eismant, K. Ghai, O. Klein, et al., Radiomolecular theranostics with fibroblast-activation-protein inhibitors and peptides, Semin. Nucl. Med. 54 (4) (2024) 537–556, https://doi.org/10.1053/j.semnuclmed.2024.05.010.

[54] Y. Liu, T. Watabe, K. Kaneda-Nakashima, Y. Shirakami, S. Naka, K. Ooe, A. Toyoshima, K. Nagata, U. Haberkorn, C. Kratochwil, et al., Fibroblast activation protein targeted therapy using [(177)Lu]FAPI-46 compared with [(225)Ac]FAPI-46 in a pancreatic cancer model, Eur. J. Nucl. Med. Mol. Imag. 49 (3) (2022) 871–880, https://doi.org/10.1007/s00259-021-05554-2. From NLM Medline.

[55] A. Shirpour, A. Hadadi, S. Zolghadri, S. Vosoughi, S. Rajabifar, Preclinical evaluation of [13xLa]La-FAP-2286 as a novel theranostic agent for tumors expressing fibroblast activation protein, Sci. Rep. 15 (1) (2025), https://doi.org/10.1038/s41598-025-91716-3.

[56] R.J. Hicks, Are FAP theranostics really happening? Will radiochemistry or biology win? J. Nucl. Med. 00 (00) (2025) https://doi.org/10.2967/jnumed.124.267547.

[57] G. Vauquelin, Effects of target binding kinetics on in vivo drug efficacy: Koff, kon and rebinding, Br. J. Pharmacol. 173 (15) (2016) 2319–2334, https://doi.org/10.1111/bph.13504.

[58] K. Andersson, M.D. Hämäläinen, Replacing affinity with binding kinetics in QSAR studies resolves otherwise confounded effects, J. Chemom. 20 (8–10) (2006) 370–375, https://doi.org/10.1002/cem.1010.

[59] D.C. Swinney, The role of binding kinetics in therapeutically useful drug action, Curr. Opin. Drug Discov. Dev 12 (1) (2009) 31–39. Review. Scopus.

[60] J.I. Venäläinen, J.A. Garcia-Horsman, M.M. Forsberg, A. Jalkanen, E.A.A. Wallén, E.M. Jarho, J.A.M. Christiaans, J. Gynther, P.T. Männistö, Binding kinetics and duration of in vivo action of novel prolyl oligopeptidase inhibitors, Biochem. Pharmacol. 71 (5) (2006) 683–692, https://doi.org/10.1016/j.bcp.2005.11.029.

[61] G.K. Walkup, Z. You, P.L. Ross, E.K. Allen, F. Daryaee, M.R. Hale, J. O'Donnell, D. E. Ehmann, V.J. Schuck, E.T. Buurman, et al., Translating slow-binding inhibition kinetics into cellular and in vivo effects, Nat. Chem. Biol. 11 (6) (2015) 416–423, https://doi.org/10.1038/nchembio.1796. From NLM.

[62] R. Zhang, C.M. Barbieri, M. Garcia-Calvo, R.W. Myers, D. McLaren, M. Kavana, Moderate to high throughput in vitro binding kinetics for drug discovery, FBS 8 (2) (2016) 278–297, https://doi.org/10.2741/s462.

[63] R. Zhang, F. Monsma, The importance of drug-target residence time, Curr. Opin. Drug Discov. Dev 12 (4) (2009) 488–496. Review. Scopus.

[64] H. Lu, P.J. Tonge, Drug–target residence time: critical information for lead optimization, Curr. Opin. Chem. Biol. 14 (4) (2010) 467–474, https://doi.org/10.1016/j.cbpa.2010.06.176.

[65] R.A. Copeland, D.L. Pompliano, T.D. Meek, Drug–target residence time and its implications for lead optimization, Nat. Rev. Drug Discov. 5 (9) (2006) 730–739, https://doi.org/10.1038/nrd2082.

[66] R.A. Copeland, The drug–target residence time model: a 10-year retrospective, Nat. Rev. Drug Discov. 15 (2) (2016) 87–95, https://doi.org/10.1038/nrd.2015.18.

[67] R.A. Copeland, The dynamics of drug-target interactions: drug-target residence time and its impact on efficacy and safety, Expet Opin. Drug Discov. 5 (4) (2010) 305–310, https://doi.org/10.1517/17460441003677725.

[68] K.S.S. Lee, J. Yang, J. Niu, C.J. Ng, K.M. Wagner, H. Dong, S.D. Kodani, D. Wan, C. Morisseau, B.D. Hammock, Drug-target residence time affects in vivo target occupancy through multiple pathways, ACS Cent. Sci. 5 (9) (2019) 1614–1624, https://doi.org/10.1021/acscentsci.9b00770. From NLM PubMed-not-MEDLINE.

[69] H. Lu, J.N. Iuliano, P.J. Tonge, Structure-kinetic relationships that control the residence time of drug-target complexes: insights from molecular structure and dynamics, Curr. Opin. Chem. Biol. 44 (2018) 101–109, https://doi.org/10.1016/j.cbpa.2018.06.002. From NLM Medline.

[70] R.H.A. Folmer, Drug target residence time: a misleading concept, Drug Discov. Today 23 (1) (2018) 12–16, https://doi.org/10.1016/j.drudis.2017.07.016. From NLM Medline.

[71] M. Cortesi, R. Guerrini, C. Roccatello, S. Pacifico, V. Albanese, P. Ulivi, G. Paganelli, S. Bravaccini, FAP inhibitors: are we really using the best method to evaluate the residence time? Eur. J. Nucl. Med. Mol. Imag. 52 (2025) 3062–3065, https://doi.org/10.1007/s00259-025-07160-y.

[72] J.F. Morrison, C.T. Walsh, The behavior and significance of slow-binding enzyme inhibitors, in: Advances in Enzymology and Related Areas of Molecular Biology, 1988, pp. 201–301.

[73] R.A. Copeland, A. Basavapathruni, M. Moyer, M.P. Scott, Impact of enzyme concentration and residence time on apparent activity recovery in jump dilution analysis, Anal. Biochem. 416 (2) (2011) 206–210, https://doi.org/10.1016/j.ab.2011.05.029.

[74] K. Augustyns, L. Beroske, L. Cianni, I. De Meester, F. Elvas, N. Filippi, S. Grintsevich, M. Tanc, Y. Van Rymenant, S. Stroobants, et al., Inhibitors of Fibroblast Activation Protein, BELGIUM WO 2023/233023 A1, 2023.

[75] A. Simkova, T. Ormsby, N. Sidej, L.P. Slavetinska, J. Brynda, J. Beranova, P. Sacha, P. Majer, J. Konvalinka, Structure-activity relationship and biochemical evaluation of novel fibroblast activation protein and prolyl endopeptidase inhibitors with alpha-ketoamide warheads, Eur. J. Med. Chem. 224 (2021), https://doi.org/10.1016/j.ejmech.2021.113717. From NLM Medline.

[76] K. Augustyns, P. Van Der Veken, P. Brzeminski, I. De Meester, F. Elvas, S. Stroobants, Y. Van Rymenant, E. Verhulst, R. Pacifico, A. Fabisiak, et al., Novel Fibroblast Activation Protein Inhibitors and Medical Uses Thereof, BELGIUM WO 2025/037000 A1, 2025.

[77] P. Brzeminski, E. Verhulst, A. Fabisiak, R. Pacifico, D. Willocx, S. Peeters, A. de Groot, S. Corthaut, K. Van Meel, S. Stroobants, et al., Structure–property investigation of new "KetoFAPI" inhibitors of Fibroblast Activation Protein (FAP): discovery of highly potent, selective compounds with prolonged residence times and promising radiotheranostic potential, J. Med. Chem. 68 (20) (2025) 21739–21765, https://doi.org/10.1021/acs.jmedchem.5c02102.

[78] S. Naka, T. Watabe, T. Lindner, J. Cardinale, K. Kurimoto, M. Moore, M. Tatsumi, Y. Mori, E. Shimosegawa, F. Valla Jr., et al., One-pot and one-step automated radio-synthesis of [(18)F]AlF-FAPI-74 using a multi purpose synthesizer: a proof-of-concept experiment, EJNMMI Radiopharm. Chem. 6 (1) (2021), https://doi.org/10.1186/s41181-021-00142-z. From NLM PubMed-not-MEDLINE.

[79] F. Osterkamp, D. Zboralski, E. Schneider, C. Haase, M. Paschke, A. Hohne, J. Ungewiss, C. Smerling, U. Reineke, A. Bredenbeck, Compounds Comprising a Fibroblast Activation Protein Ligand and Use Thereof, DE WO 2021/005131 A1, 2021.

[80] F. Osterkamp, D. Zboralski, E. Schneider, C. Haase, M. Paschke, A. Hohne, J. Ungewiss, C. Smerling, U. Reineke, A. Bredenbeck, et al., Compounds Comprising A Fibroblast Activation Protein Ligand and Use Thereof, 2023. DE US 2023/0212549 A1.

[81] K. Aertgeerts, I. Levin, L. Shi, G.P. Snell, A. Jennings, G.S. Prasad, Y. Zhang, M. L. Kraus, S. Salakian, V. Sridhar, et al., Structural and kinetic analysis of the substrate specificity of human fibroblast activation protein α, J. Biol. Chem. 280 (20) (2005) 19441–19444, https://doi.org/10.1074/jbc.C500092200.

[82] S.A. Meadows, C.Y. Edosada, M. Mayeda, T. Tran, C. Quan, H. Raab, C. Wiesmann, B.B. Wolf, Ala657 and conserved active site residues promote fibroblast activation protein endopeptidase activity via distinct mechanisms of transition state stabilization, Biochemist 46 (15) (2007) 4598–4605, https://doi.org/10.1021/bi062227y.

[83] J.E. Park, M.C. Lenter, R.N. Zimmermann, P. Garin-Chesa, L.J. Old, W.J. Rettig, Fibroblast activation protein, a dual specificity serine protease expressed in reactive human tumor stromal fibroblasts, J. Biol. Chem. 274 (51) (1999) 36505–36512, https://doi.org/10.1074/jbc.274.51.36505.

[84] M.M. Bradford, A rapid and sensitive method for the quantitation of microgram quantities of protein utilizing the principle of protein-dye binding, Anal. Biochem. 72 (1976) 248–254, https://doi.org/10.1006/abio.1976.9999.

[85] A. Shevchenko, H. Tomas, J. Havli, J.V. Olsen, M. Mann, In-gel digestion for mass spectrometric characterization of proteins and proteomes, Nat. Protoc. 1 (6) (2006) 2856–2860, https://doi.org/10.1038/nprot.2006.468.

[86] M.F. Pinto, J. Sirina, N.D. Holliday, C.L. McWhirter, High-throughput kinetics in drug discovery, SLAS Discov. 29 (5) (2024), https://doi.org/10.1016/j.slasd.2024.100170. (Accessed 28 March 2025).

[87] A. De Decker, G. Vliegen, D. Van Rompaey, A. Peeraer, A. Bracke, L. Verckist, K. Jansen, R. Geiss-Friedlander, K. Augustyns, H. De Winter, et al., Novel small molecule-derived, highly selective substrates for Fibroblast Activation Protein (FAP), ACS Med. Chem. Lett. 10 (8) (2019) 1173–1179, https://doi.org/10.1021/acsmedchemlett.9b00191. From NLM.

[88] J.I. Venäläinen, R.O. Juvonen, J.A. Garcia-Horsman, E.A. Wallén, J. A. Christiaans, E.M. Jarho, J. Gynther, P.T. Männistö, Slow-binding inhibitors of prolyl oligopeptidase with different functional groups at the P1 site, Biochem. J. 382 (Pt 3) (2004) 1003–1008, https://doi.org/10.1042/bj20040992. From NLM.

[89] R.G. Duggleby, A comment on the 'jack-knife' technique for analysing enzyme-kinetic data, Biochem. J. 181 (1) (1979) 255–256, https://doi.org/10.1042/bj1810255. From NLM Medline.

[90] G. Schnapp, Y. Hoevels, R.A. Bakker, P. Schreiner, T. Klein, H. Nar, A single second shell amino acid determines affinity and kinetics of linagliptin binding to type 4 dipeptidyl peptidase and fibroblast activation protein, ChemMedChem 16 (4) (2021) 630–639, https://doi.org/10.1002/cmdc.202000591. From NLM.

[91] A. Fiser, A. Sali, ModLoop: automated modeling of loops in protein structures, Bioinform 19 (18) (2003), https://doi.org/10.1093/bioinformatics/btg362. From NLM Medline.

[92] C.J. Williams, J.J. Headd, N.W. Moriarty, M.G. Prisant, L.L. Videau, L.N. Deis, V. Verma, D.A. Keedy, B.J. Hintze, V.B. Chen, et al., MolProbity: more and better reference data for improved all-atom structure validation, Protein Sci. 27 (1) (2018) 293–315, https://doi.org/10.1002/pro.3330. From NLM Medline.

[93] R. Anandakrishnan, B. Aguilar, A.V. Onufriev, H++ 3.0: automating pK prediction and the preparation of biomolecular structures for atomistic molecular

modeling and simulations, Nucleic Acids Res. 40 (2012) W537–W541, https://doi.org/10.1093/nar/gks375. From NLM Medline.
[94] C.R. Sondergaard, M.H. Olsson, M. Rostkowski, J.H. Jensen, Improved treatment of ligands and coupling effects in empirical calculation and rationalization of pKa values, J. Chem. Theor. Comput. 7 (7) (2011) 2284–2295, https://doi.org/10.1021/ct200133y. From NLM PubMed-not-MEDLINE.
[95] M. Anderson, A. Moshnikova, D.M. Engelman, Y.K. Reshetnyak, O.A. Andreev, Probe for the measurement of cell surface pH in vivo and ex vivo, Proc. Natl. Acad. Sci. U. S. A. 113 (29) (2016) 8177–8181, https://doi.org/10.1073/pnas.1608247113. From NLM Medline.
[96] J.J. Klicić, R.A. Friesner, S.-Y. Liu, W.C. Guida, Accurate prediction of acidity constants in aqueous solution via density functional theory and self-consistent reaction field methods, J. Phys. Chem. 106 (7) (2002) 1327–1335, https://doi.org/10.1021/jp012533f.
[97] A.D. Bochevarov, M.A. Watson, J.R. Greenwood, D. M. Multiconformation Philipp, Density functional theory-based pK(a) prediction in application to large, flexible organic molecules with diverse functional groups, J. Chem. Theor. Comput. 12 (12) (2016) 6001–6019, https://doi.org/10.1021/acs.jctc.6b00805. From NLM Medline.
[98] H.S. Yu, M.A. Watson, A.D. Bochevarov, Weighted averaging scheme and local atomic descriptor for pK(a) prediction based on density functional theory, J. Chem. Inf. Model. 58 (2) (2018) 271–286, https://doi.org/10.1021/acs.jcim.7b00537. From NLM Medline.
[99] K. Zhu, K.W. Borrelli, J.R. Greenwood, T. Day, R. Abel, R.S. Farid, E. Harder, Docking covalent inhibitors: a parameter free approach to pose prediction and scoring, J. Chem. Inf. Model. 54 (7) (2014) 1932–1940, https://doi.org/10.1021/ci500118s. From NLM Medline.
[100] M. Nabeno, F. Akahoshi, H. Kishida, I. Miyaguchi, Y. Tanaka, S. Ishii, T. Kadowaki, A comparative study of the binding modes of recently launched dipeptidyl peptidase IV inhibitors in the active site, BBRC (Biochem. Biophys. Res. Commun.) 434 (2) (2013) 191–196, https://doi.org/10.1016/j.bbrc.2013.03.010. From NLM Medline.
[101] D. Zboralski, A. Hoehne, A. Bredenbeck, A. Schumann, M. Nguyen, E. Schneider, J. Ungewiss, M. Paschke, C. Haase, J.L. von Hacht, et al., Preclinical evaluation of FAP-2286 for fibroblast activation protein targeted radionuclide imaging and therapy, Eur. J. Nucl. Med. Mol. Imag. 49 (11) (2022) 3651–3667, https://doi.org/10.1007/s00259-022-05842-5. From NLM.
[102] L. Zhang, D. Lin, X. Sun, U. Curth, C. Drosten, L. Sauerhering, S. Becker, K. Rox, R. Hilgenfeld, Crystal structure of SARS-CoV-2 main protease provides a basis for design of improved alpha-ketoamide inhibitors, Science 368 (6489) (2020) 409–412, https://doi.org/10.1126/science.abb3405. From NLM Medline.
[103] E. Awoonor-Williams, A.A.A. Abu-Saleh, Covalent and non-covalent binding free energy calculations for peptidomimetic inhibitors of SARS-CoV-2 main protease, Phys. Chem. Chem. Phys. 23 (11) (2021) 6746–6757, https://doi.org/10.1039/d1cp00266j. From NLM Medline.
[104] L. Hedstrom, Serine protease mechanism and specificity, Chem. Rev. 102 (12) (2002) 4501–4524, https://doi.org/10.1021/cr000033x. From NLM Medline.
[105] K. Aertgeerts, S. Ye, M.G. Tennant, M.L. Kraus, J. Rogers, B.C. Sang, R.J. Skene, D. R. Webb, G.S. Prasad, Crystal structure of human dipeptidyl peptidase IV in complex with a decapeptide reveals details on substrate specificity and tetrahedral intermediate formation, Protein Sci. 13 (2) (2004) 412–421, https://doi.org/10.1110/ps.03460604. From NLM Medline.
[106] R. Wilcken, M.O. Zimmermann, A. Lange, A.C. Joerger, F.M. Boeckler, Principles and applications of halogen bonding in medicinal chemistry and chemical biology, J. Med. Chem. 56 (4) (2013) 1363–1388, https://doi.org/10.1021/jm3012068. From NLM Medline.
[107] S. Benramdane, J. De Loose, N. Filippi, M. Espadinha, O. Beyens, Y.V. Rymenant, L. Dirkx, M. Bozdag, P.B. Feijens, K. Augustyns, et al., Highly selective inhibitors of dipeptidyl peptidase 9 (DPP9) derived from the clinically used DPP4-Inhibitor vildagliptin, J. Med. Chem. 66 (18) (2023) 12717–12738, https://doi.org/10.1021/acs.jmedchem.3c00609. From NLM Medline.
[108] M.J. Roy, S. Winkler, S.J. Hughes, C. Whitworth, M. Galant, W. Farnaby, K. Rumpel, A. Ciulli, SPR-measured dissociation kinetics of PROTAC ternary complexes influence target degradation rate, ACS Chem. Biol. 14 (3) (2019) 361–368, https://doi.org/10.1021/acschembio.9b00092. From NLM Medline.
[109] O. Kartal, F. Andres, M.P. Lai, R. Nehme, K. Cottier, waveRAPID-A robust assay for high-throughput kinetic screens with the creoptix WAVEsystem, SLAS Discov. 26 (8) (2021) 995–1003, https://doi.org/10.1177/24725552211013827. From NLM Medline.
[110] K.L. Williams, S. Guerrero, Y. Flores-Garcia, D. Kim, K.S. Williamson, C. Siska, P. Smidt, S.Z. Jepson, K. Li, S.M. Dennison, et al., A candidate antibody drug for prevention of malaria, Nat. Med. 30 (1) (2024) 117–129, https://doi.org/10.1038/s41591-023-02659-z. From NLM Medline.
[111] T. Rossetti, J. Ferreira, L. Ghanem, H. Buck, C. Steegborn, R.W. Myers, P. T. Meinke, L.R. Levin, J. Buck, Assessing potency and binding kinetics of soluble adenylyl cyclase (sAC) inhibitors to maximize therapeutic potential, Front. Physiol. 13 (2022), https://doi.org/10.3389/fphys.2022.1013845. From NLM PubMed-not-MEDLINE.
[112] M. Kumar, R.G. Lowery, A high-throughput method for measuring drug residence time using the transcreener ADP assay, SLAS Discov. 22 (7) (2017) 915–922, https://doi.org/10.1177/2472555217695080. From NLM.
[113] Y. Xie, J. Ma, W. Tang, Y. Zhang, C. Zhang, Y. Chen, Efficacy and safety evaluation of 177Lu-FAP-2286 in the treatment of advanced lung cancer, Clin. Nucl. Med. 49 (9) (2024) 830–837, https://doi.org/10.1097/RLU.0000000000005297. From NLM Medline.
[114] S.S. Banihashemian, M.E. Akbari, E. Pirayesh, G. Divband, A. Abolhosseini Shahrnoy, R. Nami, S.M. Mazidi, M. Nasiri, Feasibility and therapeutic potential of [(177)Lu]Lu-FAPI-2286 in patients with advanced metastatic sarcoma, Eur. J. Nucl. Med. Mol. Imag. 52 (1) (2024) 237–246, https://doi.org/10.1007/s00259-024-06795-7. From NLM Medline.
[115] A. Galbiati, A. Zana, M. Bocci, J. Millul, A. Elsayed, J. Mock, D. Neri, S. Cazzamalli, A dimeric FAP-targeting small-molecule radioconjugate with high and prolonged tumor uptake, J. Nucl. Med. 63 (12) (2022) 1852–1858, https://doi.org/10.2967/jnumed.122.264036. From NLM Medline.
[116] A. Galbiati, M. Bocci, S. Gervasoni, D. Ravazza, E. Prodi, J. Mock, G. Malloci, E. Gilardoni, D. Neri, S. Cazzamalli, Development of multivalent OncoFAP derivatives for the tumor-targeted delivery of theranostic radionuclides, J. Nucl. Med. 65 (supplement 2) (2024), 241121-241121.
[117] X.Y. Cui, Z. Li, Z. Kong, Y. Liu, H. Meng, Z. Wen, C. Wang, J. Chen, M. Xu, Y. Li, et al., Covalent targeted radioligands potentiate radionuclide therapy, Nature 630 (8015) (2024) 206–213, https://doi.org/10.1038/s41586-024-07461-6. From NLM Medline.
[118] Y. Wu, X. Wang, X. Sun, X. Gao, S. Zhang, J. Shen, H. Tian, X. Chen, H. Huang, S. Jiang, et al., Fibroblast activation protein targeting radiopharmaceuticals: from drug design to clinical translation, Acta Pharm. Sin. B (2025), https://doi.org/10.1016/j.apsb.2025.07.009.
[119] T.Y. Tsai, T.K. Yeh, X. Chen, T. Hsu, Y.C. Jao, C.H. Huang, J.S. Song, Y.C. Huang, C.H. Chien, J.H. Chiu, et al., Substituted 4-carboxymethylpyroglutamic acid diamides as potent and selective inhibitors of fibroblast activation protein, J. Med. Chem. 53 (18) (2010) 6572–6583, https://doi.org/10.1021/jm1002556. From NLM Medline.
[120] T. Tran, C. Quan, C.Y. Edosada, M. Mayeda, C. Wiesmann, D. Sutherlin, B.B. Wolf, Synthesis and structure-activity relationship of N-acyl-Gly-, N-acyl-Sar- and N-blocked-boroPro inhibitors of FAP, DPP4, and POP, Bioorg. Med. Chem. Lett. 17 (5) (2007) 1438–1442, https://doi.org/10.1016/j.bmcl.2006.11.072. From NLM Medline.
[121] S.E. Poplawski, J.H. Lai, Y. Li, Z. Jin, Y. Liu, W. Wu, Y. Wu, Y. Zhou, J. L. Sudmeier, D.G. Sanford, et al., Identification of selective and potent inhibitors of fibroblast activation protein and prolyl oligopeptidase, J. Med. Chem. 56 (9) (2013) 3467–3477, https://doi.org/10.1021/jm400351a. From NLM Medline.
[122] S.E. Poplawski, R.M. Hallett, M.H. Dornan, K.E. Novakowski, S. Pan, A. P. Belanger, Q.D. Nguyen, W. Wu, A.E. Felten, Y. Liu, et al., Preclinical development of PNT6555, a boronic acid-based, fibroblast activation protein-alpha (FAP)-targeted radiotheranostic for imaging and treatment of FAP-positive tumors, J. Nucl. Med. 65 (1) (2024) 100–108, https://doi.org/10.2967/jnumed.123.266345. From NLM Medline.
[123] P. Kuzmic, Application of the “Kobs” Method for the Study of tight-binding Reversible Inhibitors, 2022.